applied sciences

MDPI

Article

Indirect Damage Identification Method for Railway Bridges Based on Train Response Sensitivity

Sheng Zhang [1], Yandong Dong [1], An Gong [2,*] and Jilin Hou [2]

[1] China Energy Transport Technology Research Institute Co., Ltd., Beijing 100089, China; 20105736@ceic.com (S.Z.); 11092802@ceic.com (Y.D.)
[2] Department of Civil Engineering, Dalian University of Technology, Dalian 116024, China; houjilin@dlut.edu.cn
* Correspondence: 22306074@mail.dlut.edu.cn

Abstract

For heavy-haul railway bridges that suffer from stiffness degradation and structural damage under long-term high-axle-load service conditions, conventional direct bridge damage identification methods are restricted by the high deployment and maintenance costs of dense sensor systems. To address this problem, this paper proposes an indirect bridge damage identification method based on train response sensitivity. A vehicle-track-bridge coupled dynamic model accounting for track irregularity excitation is established. The sensitivity equation for damage inversion is formulated by taking the pitch angular velocity of the leading vehicle as the key train response metric. Tikhonov regularization is introduced to alleviate the ill-posedness of the inverse problem and is further combined with non-negativity constraints on damage factors and a dynamic locking strategy. On this basis, a joint identification scheme relying on vehicle-bridge interaction is developed by incorporating bridge mid-span acceleration responses into the inversion framework. Three types of numerical scenarios, namely single damage, multiple damage, and minor damage, are designed to compare different inversion strategies and systematically investigate the influences of train speed, measurement noise, and track irregularity level on identification performance. The results demonstrate that physical constraints effectively suppress spurious damage and improve the accuracy of both damage localization and severity quantification. The joint identification method based on vehicle-bridge interaction significantly outperforms the approach using only train response in terms of minor damage detection capability and noise robustness, and can stably locate the primary damage sites within the speed range of 40–80 km/h. This method enables a hierarchical monitoring strategy integrating preliminary onboard screening with refined bridge-based diagnosis, offering a cost-effective technical solution for the structural health monitoring of heavy-haul railway bridges.

Keywords: heavy-haul railway; bridge damage identification; train response; vehicle-bridge interaction; Tikhonov regularization

Check for updates

Academic Editor: Krzysztof Zboiński

Received: 5 September 2026
Revised: 17 October 2026
Accepted: 19 October 2026
Published: 26 October 2026

Copyright: © 2026 by the authors. Licensee MDPI, Basel, Switzerland. This article is an open access article distributed under the terms and conditions of the Creative Commons Attribution (CC BY) license.

1. Introduction

Heavy-haul railways play an important role in China's freight transportation system owing to their high transport capacity and relatively low operating costs and energy consumption [1–3]. By the end of 2024, nearly 11,000 km of heavy-haul railways were in operation in China. Heavy-haul freight trains with a 25 t axle load and a gross trailing

load of 10,000 t have been in regular commercial operation on the Shuozhou–Huanghua Railway [4]. Under repeated heavy axle loads, railway bridges may develop excessive vibrations, abnormal deflections, and cracking, potentially threatening operational safety. Therefore, efficient and reliable bridge damage identification is essential for ensuring the safe operation and effective maintenance of heavy-haul railways.

Existing bridge damage identification methods can generally be divided into direct and indirect approaches. Direct methods identify structural deterioration from measured bridge responses. Early studies primarily employed natural frequencies as damage indicators, although their sensitivity to minor and localized damage is limited [5]. Subsequent studies introduced modal strain energy, flexibility, and flexibility curvature to improve damage localization [6–9]. Wavelet analysis has also been used to extract damage-related features from non-stationary responses [10], while long short-term memory (LSTM) networks have demonstrated potential for data-driven damage classification [11]. Despite these advances, direct monitoring generally requires permanently installed sensors and associated data acquisition systems. For extensive heavy-haul railway networks, installation and maintenance costs restrict the widespread deployment of such monitoring systems.

Indirect bridge health monitoring provides a potentially cost-effective alternative by using passing trains as mobile sensing platforms to infer bridge dynamic characteristics and structural conditions. Early studies focused on extracting bridge modal information from onboard responses. Contact-point responses were subsequently introduced to suppress vehicle-related dynamic components and improve the identification of bridge modes [12]. Dual Kalman filtering combined with singular spectrum analysis was employed to reduce the influence of surface irregularities [13]. Damage identification methods based on contact-point responses [14] and statistical features of dynamic displacement [15] were also developed. To improve inversion stability, Krishnanunni and Rao combined Tikhonov regularization with signal averaging to mitigate the effects of measurement noise and surface roughness [16]. Zhan et al. [17] applied differential processing to contact-point responses from repeated crossings to reduce irregularity-induced interference and support multiple-damage identification. These studies have improved damage-sensitive feature extraction and inversion robustness, but reliable identification under complex operating conditions remains challenging.

For railway bridges, the coupled effects of train configuration, track irregularities, and bridge dynamics introduce additional challenges. Zhan et al. [18] investigated sensitivity-based bridge damage identification using train-induced responses. Carnevale et al. [19] examined the influence of sensor locations and frequency bands using a coupled train–track–bridge model, highlighting the potential of leading-bogie responses for damage detection and the adverse effects of track irregularities. For heavy-haul railway bridges, Shi et al. [20] established sensitivity-based damage identification equations using bogie responses. They subsequently proposed a multistage framework integrating time-domain correlation-based denoising, empirical mode decomposition, and sliding-window analysis for damage detection, localization, and severity assessment [21]. These studies demonstrate the feasibility of identifying railway bridge damage from train-related responses [22]. Nevertheless, accurately quantifying minor damage remains difficult when track irregularities and measurement noise coexist.

Recent developments in output-only modal analysis and crowdsensing have further demonstrated the potential of mobile measurements for large-scale bridge condition assessment [23–26]. Complementary monitoring approaches [27,28] and physics-constrained data-driven methods [29] have also broadened the available methodological options. However, two challenges remain particularly important for sensitivity-based damage identification in heavy-haul railway bridges. First, minor stiffness reductions

produce weak damage-related features that can be obscured by track irregularities, measurement noise, and variations in operating conditions. Second, damage inversion based on a single onboard response may be ill-conditioned, resulting in amplified measurement errors and unstable estimates of damage severity. These limitations motivate the development of a constrained inversion framework that combines complementary vehicle and bridge responses to improve damage identifiability while limiting the need for permanent bridge instrumentation.

To address these challenges, this study proposes a sensitivity-based damage identification method for simply supported heavy-haul railway bridges using coupled vehicle–bridge responses. First, a vehicle–track–bridge dynamic model incorporating track-irregularity excitation is established, and damage sensitivity equations are formulated using the pitch angular velocity of the leading vehicle. Tikhonov regularization is adopted to stabilize the inverse problem, while non-negativity constraints and a dynamic locking strategy are introduced to restrict unreasonable iterative updates of damage factors. The mid-span acceleration response of the bridge is then incorporated to provide complementary information for joint vehicle–bridge damage identification. Numerical studies involving single, multiple, and minor damage scenarios are conducted to assess the identification performance and its sensitivity to measurement noise. The proposed framework integrates damage-sensitive onboard measurements, constrained inversion, and limited bridge responses, supporting a staged monitoring strategy in which onboard measurements enable preliminary damage screening and bridge responses provide additional information for damage localization and severity estimation.

2. Vehicle–Track–Bridge Coupled Dynamic Model

A coupled vehicle–track–bridge model is established to reproduce the dynamic interaction between the heavy-haul train, the track system, and a simply supported railway bridge. The model is deliberately restricted to one 32 m span, which is consistent with the single-span identification cases considered in this study. The bridge is discretized into 50 two-node Euler–Bernoulli beam elements and divided into 10 damage zones. Each zone contains five consecutive elements and is assigned one damage factor, so that the inverse problem contains ten unknown damage parameters.

2.1. Vehicle Model and Assumptions

The vehicle model follows the established 10-degree-of-freedom formulation proposed by Zhai et al. [30]. Each vehicle is represented by a rigid car body, two rigid bogies, and four wheelsets. The car body has one vertical displacement degree of freedom and one pitch rotation degree of freedom. Each bogie has one vertical displacement degree of freedom and one pitch rotation degree of freedom, giving four bogie degrees of freedom in total. The four wheelsets contribute four vertical displacement degrees of freedom. The train used in the simulation consists of one leading HXD1 electric locomotive followed by four C80 heavy-haul wagons.

The following assumptions are adopted. The car bodies, bogies, and wheelsets are treated as rigid bodies; their mass distributions are symmetric about the corresponding centers of mass; the vibration amplitudes are small; the primary and secondary suspensions are represented by linear spring–damper elements; longitudinal vehicle motion is neglected because the present analysis focuses on vertical and pitch dynamics; and the train travels at a constant speed. These assumptions retain the dominant vertical interaction mechanisms while keeping the forward model computationally tractable.

For vehicle i, the equations of motion are written in matrix form as follows:

$$\boldsymbol{M}_{\mathrm{vv}i}\ddot{\boldsymbol{X}}_{\mathrm{vv}i} + \boldsymbol{C}_{\mathrm{vv}i}\dot{\boldsymbol{X}}_{\mathrm{vv}i} + \boldsymbol{K}_{\mathrm{vv}i}\boldsymbol{X}_{\mathrm{vv}i} = \boldsymbol{F}_{\mathrm{v}i} \quad (1)$$

Here, $\boldsymbol{M}_{\mathrm{vv}i}$, $\boldsymbol{C}_{\mathrm{vv}i}$, $\boldsymbol{K}_{\mathrm{vv}i}$ are the vehicle mass, damping, and stiffness matrices, respectively; $\boldsymbol{X}_{\mathrm{vv}i}$, $\dot{\boldsymbol{X}}_{\mathrm{vv}i}$, $\ddot{\boldsymbol{X}}_{\mathrm{vv}i}$ denote the displacement, velocity, and acceleration vectors; and $\boldsymbol{F}_{\mathrm{v}i}$ is the external force vector generated by gravity, suspension forces, and wheel–rail contact forces.

The train model is shown in Figure 1, and the corresponding parameters of each train type are listed in Table 1.

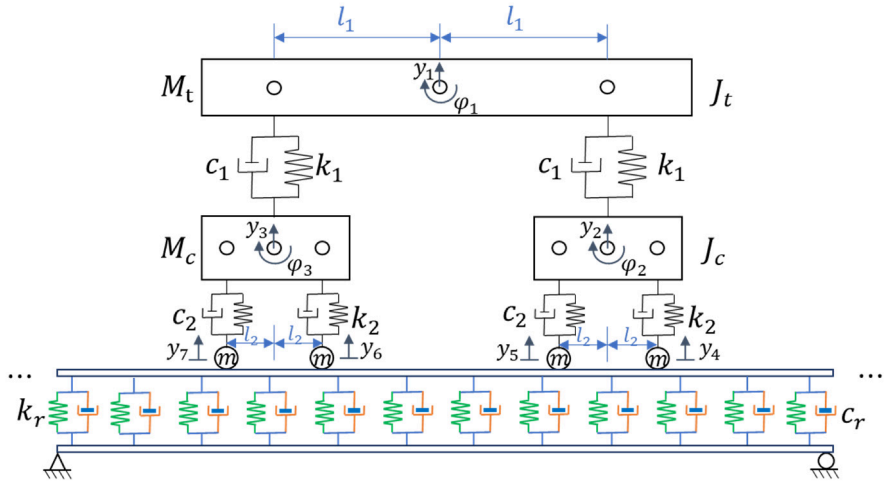


Figure 1. 10-DOF Train Model.

Table 1. Parameters of the HXD1 locomotive and C80 wagon models.

Parameter	HXD1	C80
Vehicle length (m)	17.5	12
Overall wheelbase (m)	9.3	8.2
Bogie wheelbase (m)	2.8	1.83
Car-body mass (kg)	90,400	90,400
Bogie mass (kg)	4800	4800
Wheelset mass (kg)	1171	1171
Car-body pitch inertia (kg·m^2)	2.1×10^6	9.84×10^5
Bogie pitch inertia (kg·m^2)	3500	1700
Primary suspension stiffness (N/m)	2×10^6	2×10^6
Primary suspension damping (N·s/m)	8×10^4	8×10^4
Secondary suspension stiffness (N/m)	4.895×10^6	4.895×10^6
Secondary suspension damping (N·s/m)	1×10^5	1×10^5

2.2. Track and Bridge Finite-Element Model

The numerical model is based on a representative 32 m simply supported prestressed concrete girder bridge used in Chinese heavy-haul railways. Xiao et al. [31] investigated the dynamic responses of this bridge through field measurements under heavy-haul train loading. The reported concrete elastic modulus of 35.5 GPa and density of 2500 kg/m^3 are consistent with the values adopted in the present study. Furthermore, Song et al. [32] conducted field measurements on a 32 m simply supported prestressed concrete railway bridge under C80 freight-train loading at 60 km/h, providing additional engineering support for the selected bridge configuration and operating conditions.

Based on these engineering characteristics, the bridge is modeled as a simply supported Euler–Bernoulli beam to characterize its global vertical bending response. Each node has a vertical displacement and a rotation about the transverse axis. The vertical displacements at the two supports are constrained, whereas the end rotations remain free, corresponding to standard simply supported boundary conditions. The rail is also represented by an Euler–Bernoulli beam and is coupled to the bridge deck through equivalent linear spring–damper elements. Thus, the track is explicitly included in the forward model rather than treated solely as an external excitation source. This simplified representation focuses on the dominant vertical dynamic behavior of a single span without explicitly modeling the detailed sleeper–ballast system or three-dimensional structural effects.

After assembly of the bridge and rail finite-element matrices, the coupled track–bridge equations can be written in block form as follows:

$$\begin{bmatrix} \boldsymbol{M}_{\mathrm{rr}} & 0 \\ 0 & \boldsymbol{M}_{\mathrm{bb}} \end{bmatrix} \begin{bmatrix} \ddot{\boldsymbol{X}}_{\mathrm{r}} \\ \ddot{\boldsymbol{X}}_{\mathrm{b}} \end{bmatrix} + \begin{bmatrix} \boldsymbol{C}_{\mathrm{rr}} & \boldsymbol{C}_{\mathrm{rb}} \\ \boldsymbol{C}_{\mathrm{br}} & \boldsymbol{C}_{\mathrm{bb}} \end{bmatrix} \begin{bmatrix} \dot{\boldsymbol{X}}_{\mathrm{r}} \\ \dot{\boldsymbol{X}}_{\mathrm{b}} \end{bmatrix} + \begin{bmatrix} \boldsymbol{K}_{\mathrm{rr}} & \boldsymbol{K}_{\mathrm{rb}} \\ \boldsymbol{K}_{\mathrm{br}} & \boldsymbol{K}_{\mathrm{bb}} \end{bmatrix} \begin{bmatrix} \boldsymbol{X}_{\mathrm{r}} \\ \boldsymbol{X}_{\mathrm{b}} \end{bmatrix} = \begin{bmatrix} \boldsymbol{F}_{\mathrm{r}} \\ 0 \end{bmatrix} \tag{2}$$

The subscripts r and b denote the rail and bridge, respectively, and K_f and C_f are the fastener stiffness and damping matrices. The wheel–rail contact condition enforces displacement compatibility at the moving contact locations and transfers the wheel loads to the rail. Hermite interpolation is used to evaluate the rail and bridge response at the moving wheel positions.

The bridge damage factors are defined zone-wise. Let a_z denote the damage factor of zone z, where $a_z = 0$ represents the intact state and $a_z = 1$ represents complete loss of the corresponding bending stiffness. The bridge stiffness matrix is assembled as follows:

$$K_\beta(\alpha) = K_{\beta,0} - \sum_{z=1}^{Z} \alpha_z K_{\beta,z},\ z = 1, 2, \ldots, 10. \tag{3}$$

In the default mesh, element-to-zone mapping is explicit: elements 1–5 form zone 1, elements 6–10 form zone 2, and so forth until elements 46–50 form zone 10. The same zone damage factor is applied to the five elements within each zone. The bridge structure is discretized into N elements using the finite element method.

The detailed parameters for the track and bridge are presented in Table 2.

Table 2. Train model parameters.

Parameter	Value	
	Bridge	**Track**
Elastic modulus (Pa)	3.55×10^{10}	2.1×10^{11}
Second moment of area (m^4)	14.341	3.217×10^{-5}
Cross-sectional area (m^2)	13.955	7.745×10^{-3}
Density (kg/m^3)	2500	7850
Structural damping ratio	0.03	0.01
Fastener stiffness (N/m)	-	1.2×10^8
Fastener damping (N·s/m)	-	7.5×10^4
Fastener spacing (m)	-	0.64
mesh	50 elements; 0.64 m per element	50 elements; 0.64 m per element

2.3. Track Irregularity and Numerical Integration

Track irregularity is introduced as a spatial excitation. The prescribed FRA grade-5 vertical irregularity spectrum is discretized on a spatial grid with $\triangle_x$ = 0.01 m. A deterministic realization is generated using random phases and the fixed roughness seed 123, so that all damage cases use the same track realization. In general form, the spatial profile can be represented by:

$$\omega(x) = \sqrt{2}\sum_{k=1}^{N} \sqrt{S(\omega_k)\Delta\omega}\cos(\omega_k x + \phi_k) \tag{4}$$

where $S(\omega_k)$ is the prescribed spatial power spectral density, ω_k is the spatial angular frequency, and $\Delta\omega$ is the frequency increment. The same irregularity realization is used for the intact and damaged forward calculations so that the damage response is not contaminated by a change in the excitation realization.

The vertical track irregularity obtained via the trigonometric series method is presented in Figure 2.

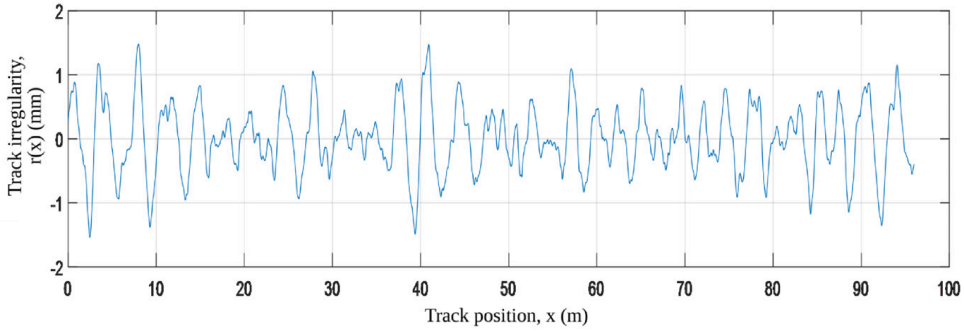


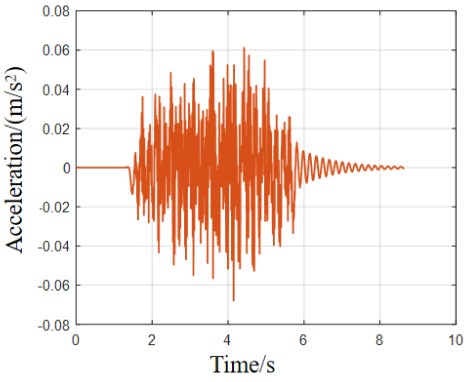
Figure 2. Track irregularities generated by the trigonometric series method.

The vehicle, rail, and bridge equations are coupled by the moving wheel–rail contact conditions and integrated in the time domain using the Newmark average-acceleration method. The parameters β = 0.25 and γ = 0.50 are used. The train speed is 60 km/h, the sampling frequency is 400 Hz, and the time step is $\triangle_t$ = 1/fs. The initial displacement and velocity vectors are zero, while the initial acceleration is obtained from the assembled equilibrium equations.

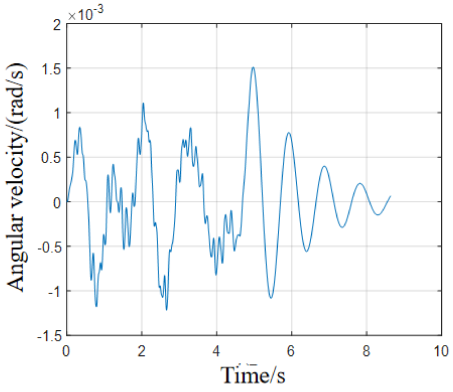
$$M_c\ddot{q}_c + C_c\dot{q}_c + K_c(\alpha)q_c = F_c(t), \tag{5}$$

The subscript c denotes the assembled vehicle–track–bridge system. For the Newmark average-acceleration scheme, $a_0 = 1/(\beta\Delta t^2)$ and $a_1 = \gamma/(\beta\Delta t)$, and the effective matrix at each time step is $A_n = K_n + a_0M_n + a_1C_n$. The moving wheel–rail projection is rebuilt at the current wheel positions; the same effective matrix and factorization are used for the forward state and the tangent columns. The leading-vehicle body pitch angular velocity and the bridge mid-span vertical acceleration are extracted on the same time grid. Gaussian white noise with an RMS value equal to 5% of the corresponding clean signal RMS is added independently to the two measured response channels.

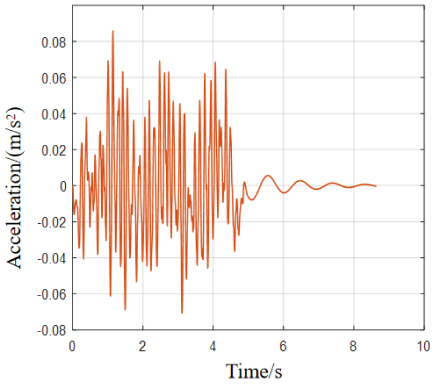
Based on the above conditions, the dynamic responses of the vehicle-track-bridge coupled system are calculated, and some typical results are shown in Figure 3.



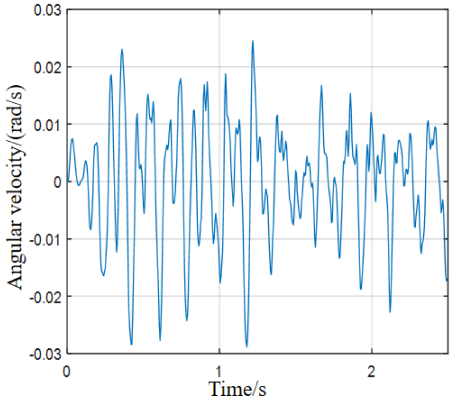
(**a**) bridge mid-span acceleration



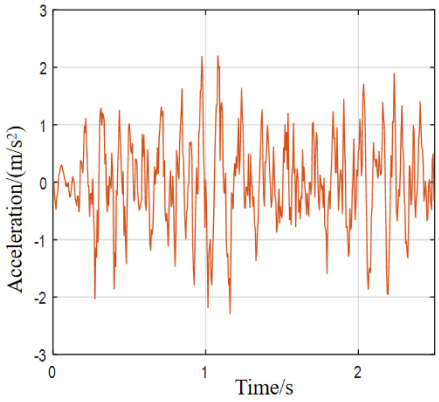
(**b**) leading car body pitch angular velocity



(**c**) leading car body vertical acceleration



(**d**) leading car front bogie pitch angular velocity



(**e**) leading car front bogie vertical acceleration

Figure 3. Typical dynamic response of the train-track-bridge coupled system.

By comparing with the model results in reference [19], it can be seen that the vibration responses at the midspan of the train and bridge are basically consistent in terms of amplitude fluctuation range and overall trend. The slight deviations are caused by random track irregularities and also related to differences in modeling details such as element division accuracy and damping parameter values in this study.

3. Derivation of Sensitivity Equations

When a train passes over a bridge, the dynamic responses of the vehicle-track-bridge coupled system depend not only on the train operating conditions but also on the structural parameters of the bridge and track. Local damage to the bridge or track alters its structural properties, such as stiffness, and consequently changes the dynamic responses of the cou-

pled system. Therefore, the response data obtained during train operation can be regarded as an indirect reflection of the structural state and provide a basis for damage identification.

The bridge finite-element mesh contains 50 elements, which are grouped into 10 consecutive damage zones. The zone-level damage factor is denoted by a_i (i = 1, …, 10), and the same factor is applied to the five elements within zone i. The response at the j-th sampling point, or at the j-th time sample, is denoted by y_j. Each response sample is a nonlinear function of the 10 zone-level factors and can be written in the form shown in Equation (6), with n = 10.

$$u_j = f_j(\alpha_1, \alpha_2, \ldots\ldots, \alpha_n)\ 1 \le j \le m \tag{6}$$

where $\boldsymbol{m}$ represents the total number of all sampling points (or all observed values).

Direct analytical determination of the damage factors of individual elements from the above multivariate function is generally difficult because f_j represents a nonlinear and complex mapping between the damage factors and the system response. Therefore, to facilitate the analysis, a multivariate Taylor series expansion is performed about the assumed initial values $(\alpha_{1,0}, \alpha_{2,0}, \ldots, \alpha_{n,0})$ of the bridge damage factors, yielding [33]:

$$u_j = \sum_{m_1=0}^{\infty} \sum_{m_2=0}^{\infty} \cdots \sum_{m_n=0}^{\infty} \frac{\partial^{m_1+m_2+\cdots+m_n} f_j(\alpha_{1,0}, \alpha_{2,0}, \cdots, \alpha_{n,0})}{\partial \alpha_1^{m_1} \partial \alpha_2^{m_2} \cdots \partial \alpha_n^{m_n}} \cdot \frac{(\alpha_1 - \alpha_{1,0})^{m_1} (\alpha_2 - \alpha_{2,0})^{m_2} \cdots (\alpha_n - \alpha_{n,0})^{m_n}}{m_1! m_2! \cdots m_n!} \tag{7}$$

When only the first two terms of the multivariate Taylor series expansion are retained and the higher-order terms are neglected, u_j is approximated as follows:

$$u_j = u_{j,0} + \sum_{i=1}^{n} \frac{\partial u_j}{\partial \alpha_i} (\alpha_i - \alpha_{i,0}) \tag{8}$$

where $u_{j,0} = f(\alpha_{1,0}, \alpha_{2,0}, \ldots, \alpha_{n,0})$. Equation (8) is then rewritten in incremental form:

$$\Delta u_j = \sum_{i=1}^{n} \frac{\partial u_j}{\partial \alpha_i} \Delta \alpha_i = \frac{\partial u_j}{\partial \alpha_1} \Delta \alpha_1 + \frac{\partial u_j}{\partial \alpha_2} \Delta \alpha_2 + \ldots + \frac{\partial u_j}{\partial \alpha_n} \Delta \alpha_n \tag{9}$$

where $\Delta u_j = u_j - u_{j,0}$, $\Delta \alpha = \alpha_i - \alpha_{i,0}$.

When Equation (9) is applied to each sampling point in sequence, the following set of equations is obtained:

$$\begin{cases} \Delta u_1 = \frac{\partial u_1}{\partial \alpha_1} \Delta \alpha_1 + \frac{\partial u_1}{\partial \alpha_2} \Delta \alpha_2 + \ldots + \frac{\partial u_1}{\partial \alpha_n} \Delta \alpha_n \\ \Delta u_2 = \frac{\partial u_2}{\partial \alpha_1} \Delta \alpha_1 + \frac{\partial u_2}{\partial \alpha_2} \Delta \alpha_2 + \ldots + \frac{\partial u_2}{\partial \alpha_n} \Delta \alpha_n \\ \vdots \\ \Delta u_m = \frac{\partial u_m}{\partial \alpha_1} \Delta \alpha_1 + \frac{\partial u_m}{\partial \alpha_2} \Delta \alpha_2 + \ldots + \frac{\partial u_m}{\partial \alpha_n} \Delta \alpha_n \end{cases} \tag{10}$$

Equation (10) is rearranged into matrix form:

$$\begin{bmatrix} \Delta u_1 \\ \Delta u_2 \\ \vdots \\ \Delta u_m \end{bmatrix}_{m \times 1} = \begin{bmatrix} \frac{\partial u_1}{\partial \alpha_1} & \frac{\partial u_1}{\partial \alpha_2} & \cdots & \frac{\partial u_1}{\partial \alpha_n} \\ \frac{\partial u_2}{\partial \alpha_1} & \frac{\partial u_2}{\partial \alpha_2} & \cdots & \frac{\partial u_2}{\partial \alpha_n} \\ \vdots & \vdots & \ddots & \vdots \\ \frac{\partial u_m}{\partial \alpha_1} & \frac{\partial u_m}{\partial \alpha_2} & \cdots & \frac{\partial u_m}{\partial \alpha_n} \end{bmatrix}_{m \times n} \begin{bmatrix} \Delta \alpha_1 \\ \Delta \alpha_2 \\ \vdots \\ \Delta \alpha_n \end{bmatrix}_{n \times 1} \tag{11}$$

which is simplified to:

$$\Delta u = S \Delta a \tag{12}$$

Here S is the response sensitivity matrix. In the present model, S has m rows and 10 columns, and its j-th column contains the response derivative with respect to the damage factor of zone j. Equation (12) is therefore the local sensitivity equation for the ten unknown zone-level factors.

Building on the response sensitivity formulation, this study develops an iterative damage identification framework for heavy-haul railway bridges using a coupled vehicle–track–bridge dynamic model. The leading vehicle's body pitch angular velocity serves as the primary onboard observation, while the bridge mid-span vertical acceleration is incorporated as a complementary response for joint identification. The proposed method combines Tikhonov regularization, physical constraints on the damage factors, and a dynamic locking strategy for damage localization and severity estimation. At each outer iteration, the simulated responses and sensitivity matrix are recalculated at the current damage estimate, and the damage factors are updated by solving the corresponding linearized inverse subproblem. The overall identification procedure is illustrated in Figure 4.

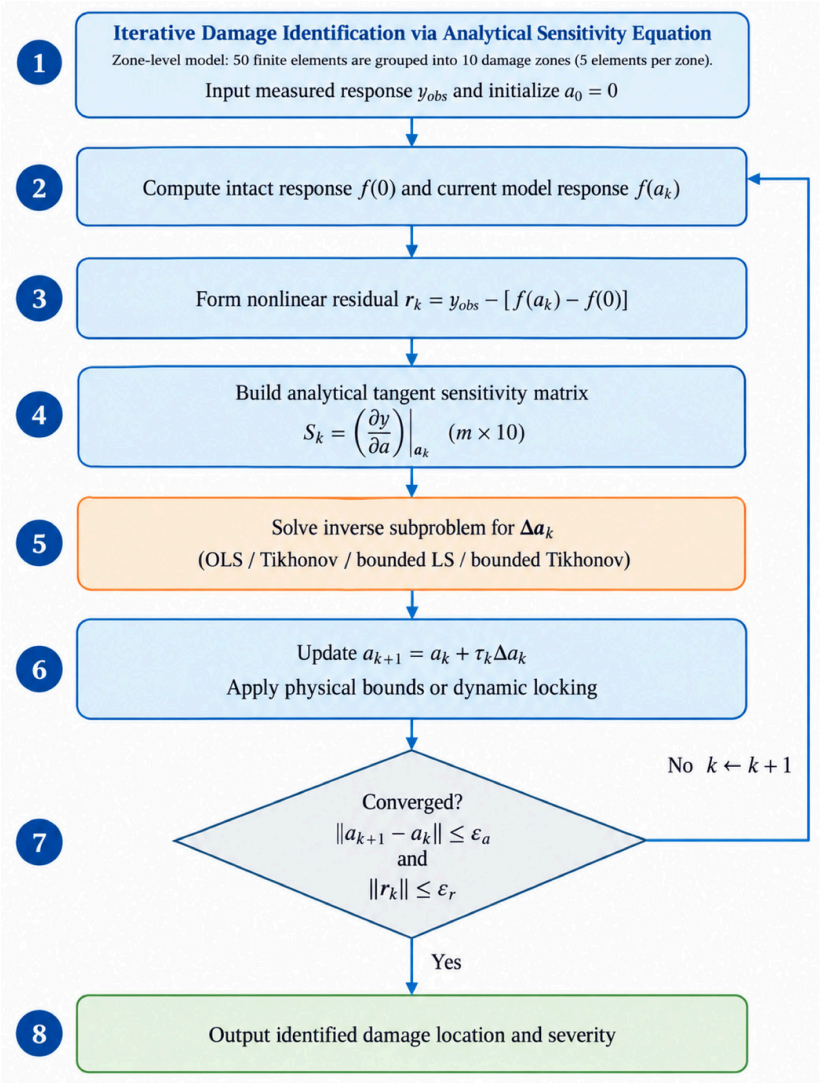


Figure 4. Flowchart of the Damage Identification Algorithm.

The specific nonlinear solution procedure is as follows: (1) establish the vehicle–track–bridge model and obtain the measured response vector; (2) initialize the damage vector a_0 and calculate the intact response f(0); (3) at outer iteration k, construct the current model $f(a_k)$ f(a_k) and calculate the residual $r_k = y_{\text{obs}} - [f(a_k) - f(0)]$; (4) recompute the analytical

discrete-time sensitivity matrix $S_k = \partial f / \partial a|_{a_k}$; (5) solve the selected inverse subproblem for $\triangle a_k$; (6) update the damage vector and apply the physical bounds or the dynamic locking rule; and (7) evaluate the stopping criteria. The outer iteration terminates when both the applied update and the nonlinear residual satisfy their prescribed tolerances, or when the maximum number of outer iterations is reached.

Analytical Tangent Sensitivity for the Zone-Level Model

The 50 finite elements are grouped into 10 damage zones, with five consecutive elements in each zone. The inverse parameter is therefore $\mathbf{a} = [a_1, \cdots, a_{10}]^{\mathrm{T}}$, and the sensitivity matrix has dimension m × 10. For zone j, the stiffness derivative is $\mathbf{K}_{s,j} = \frac{\partial \mathbf{K}}{\partial a_j} = -\sum_{e \in Z_j} \mathbf{K}_{e,0}$, whereas the mass derivative is zero. With Rayleigh damping $\mathbf{C} = \alpha^{\mathrm{R}}\mathbf{M} + \beta^{\mathrm{R}}\mathbf{K}$, the corresponding damping derivative is $\mathbf{C}_{s,j} = \beta^{\mathrm{R}}\mathbf{K}_{s,j}$ for the bridge block.

The tangent response is obtained by differentiating the Newmark-discretized coupled dynamic equation. For each damage factor a_j, the tangent state satisfies $\mathbf{M}\ddot{\mathbf{q}}_{s,j} + \mathbf{C}\dot{\mathbf{q}}_{s,j} + \mathbf{K}\mathbf{q}_{s,j} = -\mathbf{C}_{s,j}\dot{\mathbf{q}} - \mathbf{K}_{s,j}\mathbf{q}$. The same effective Newmark matrix, time step, moving wheel–rail projection, and output extraction used by the forward solve are used for this tangent solve. Thus, $S_k = \left.\frac{\partial \mathbf{y}}{\partial \mathbf{a}}\right|_{\mathbf{a}_k}$ is an analytical discrete-time tangent sensitivity, rather than a finite-difference approximation; finite differences are used only for independent verification.

The output vector y may contain the leading-vehicle body pitch angular velocity, the bridge mid-span vertical acceleration, or their stacked joint observation. In the joint case, each channel is divided by a fixed RMS scale computed from the intact reference response before stacking so that the different physical units do not determine the inversion solely through their magnitudes.

When a train passes over a bridge, the dynamic responses of the vehicle-track-bridge coupled system depend not only on the train operating conditions but also exhibit high sensitivity to variations in the structural parameters of the bridge and track. Local damage to the bridge or track alters the structural properties of the affected component, such as its stiffness, thereby inducing changes in the dynamic responses of the coupled system. Therefore, the response data acquired during train operation can be regarded as an indirect manifestation of the structural state and can provide a basis for damage identification.

4. Solution of the Sensitivity Equation

This section formulates the inverse solution of the sensitivity equation and compares four nonlinear damage-identification strategies.

The sensitivity matrix is generally rectangular, and the measured response may contain noise. Accordingly, the damage increment is first estimated by least squares. For a sensitivity matrix with full column rank, the resulting normal-equation solution is given in Equation (13). For rank-deficient cases, a singular-value-decomposition (SVD) pseudoinverse is required.

This section presents the damage identification algorithm based on sensitivity analysis, in which solving the sensitivity equation is a key step.

Since the sensitivity matrix is non-square and generally corresponds to an overdetermined system, direct inversion is mathematically infeasible. Moreover, owing to measurement noise, the system of equations generally does not admit an exact solution. Therefore, the least-squares method is employed to obtain the optimal estimate of the damage parameters in the least-squares sense. This is essentially equivalent to solving the overdetermined linear system using the Moore–Penrose pseudoinverse, and the corresponding expression can be written as follows:

$$\Delta a_k = \left[(S^k)^T S^k \right]^{-1} (S^k)^T \Delta u^k \tag{13}$$

However, it should be noted that the sensitivity equation established by the above procedure often exhibits obvious ill-posedness and ill-conditioning in practical damage identification, which is one of the key common difficulties in structural damage inversion problems.

4.1. Ill-Posedness and Ill-Conditioning of the Sensitivity Equation

(1) Ill-posedness of the sensitivity equation

The sensitivity equation constitutes a typical inverse problem. Owing to limited observational information, measurement noise, and modeling errors, the existence, uniqueness, and stability of its solution cannot always be simultaneously guaranteed. The solution is therefore highly sensitive to perturbations in the input data, resulting in an ill-posed problem.

(2) Ill-conditioning of the sensitivity equation

Strong correlations among sensitivity-matrix columns and small singular values can cause ill-conditioning, which amplifies measurement errors and destabilizes least-squares estimates.

Regularization and physically motivated constraints, including non-negative damage factors and admissible bounds, can reduce noise amplification and help exclude nonphysical estimates.

4.2. Tikhonov Regularization

Regularization methods can effectively mitigate the ill-posedness and ill-conditioning of sensitivity equations. By introducing appropriate constraints, these methods improve solution stability while incorporating prior information on damage, thereby yielding results that are more consistent with engineering practice. Common approaches include truncated singular value decomposition (TSVD) [34], (L1) regularization [35], and Bayesian methods [36], each of which has limitations in terms of parameter selection, computational complexity, or applicability.

Considering both solution stability and engineering feasibility, Tikhonov regularization is adopted in this study [37]. By introducing a norm-based penalty term, this method suppresses the excessive amplification of the solution caused by ill-conditioning and provides a good balance between stability and accuracy. In addition, its simple formulation and ease of implementation make it suitable for damage identification in complex vehicle-track-bridge coupled systems.

To stabilize the linearized least-squares inversion, a regularization penalty term λ is introduced. The resulting Tikhonov-regularized damage increment is expressed as follows:

$$\Delta\boldsymbol{\alpha}_k = \left[\left(\boldsymbol{S}^k\right)^T\boldsymbol{S}^k + \lambda\boldsymbol{I}\right]^{-1}\left(\boldsymbol{S}^k\right)^T\Delta\boldsymbol{u}^k \tag{14}$$

The regularization parameter λ_k controls the balance between the residual and increment norms in Equation (15), with r_k denoting the current nonlinear residual. A small λ_k provides insufficient suppression of noise amplification, whereas an excessively large λ_k may suppress genuine damage updates.

$$J(\Delta\alpha_k, \lambda) = \|S^k\Delta\alpha_k - \Delta u^k\|_2^2 + \lambda\|\Delta\alpha_k\|_2^2 \tag{15}$$

The L-curve method is used to select λ_k. For a logarithmic candidate grid, each candidate is evaluated with the current S_k and r_k, and the pair $(\|S_k\Delta a_k(\lambda) - r_k\|_2,\ \|\Delta a_k(\lambda)\|_2)$ is plotted in log–log coordinates. The corner with the largest discrete curvature is selected. This procedure is repeated after every outer model update because both the sensitivity spectrum and the residual change with the damage state.

4.3. Normalization and Weighting of Joint Vehicle–Bridge Responses

The vehicle pitch angular velocity and bridge acceleration have different physical units and characteristic amplitudes. Therefore, the two response blocks are nondimensionalized before they are assembled into the joint inverse problem. For response channel $q \in \{v, b\}$, where v and b denote the vehicle and bridge channels, respectively, the reference scale is defined using the corresponding intact-state response:

$$s_q = \left[\frac{1}{N_q} \sum_{i=1}^{N_q} u_{q,0}^2(t_i) \right]^{1/2} \tag{16}$$

Here, $u_{q,0}(t_i)$ denotes the intact reference response, and N_q is the number of samples in that response block. The reference scale is calculated from the intact-state response and held fixed throughout the nonlinear iterations.

At iteration k, let $r_{q,k}$ denote the current response residual and $S_{q,k}$ its corresponding sensitivity matrix. The same scale is applied to both quantities:

$$\widetilde{\mathbf{r}}_{q,k} = \frac{\mathbf{r}_{q,k}}{s_q}, \ \widetilde{\mathbf{S}}_{q,k} = \frac{\mathbf{S}_{q,k}}{s_q}. \tag{17}$$

The joint residual vector and sensitivity matrix are consequently assembled as

$$\widetilde{\mathbf{r}}_k = \begin{bmatrix} \widetilde{\mathbf{r}}_{v,k} \\ \widetilde{\mathbf{r}}_{b,k} \end{bmatrix}, \ \widetilde{\mathbf{S}}_k = \begin{bmatrix} \widetilde{\mathbf{S}}_{v,k} \\ \widetilde{\mathbf{S}}_{b,k} \end{bmatrix}. \tag{18}$$

The regularized joint objective can then be expressed as

$$J_k(\Delta\mathbf{a}) = \left\| \widetilde{\mathbf{r}}_{v,k} - \widetilde{\mathbf{S}}_{v,k}\Delta\mathbf{a} \right\|_2^2 + \left\| \widetilde{\mathbf{r}}_{b,k} - \widetilde{\mathbf{S}}_{b,k}\Delta\mathbf{a} \right\|_2^2 + \lambda_k \|\Delta\mathbf{a}\|_2^2 \tag{19}$$

This formulation assigns equal coefficients to the two dimensionless residual blocks, corresponding to weights of s_v^{-2} and s_b^{-2} in the original physical units. Both response channels are extracted on the common time grid described in Section 2.3. For the equal-length records considered here, $N_v = N_b$, so neither block receives additional weight merely because it contains more samples. The vehicle-only and bridge-only objectives retain the corresponding normalized block, whereas the joint objective includes both blocks.

Reference-RMS normalization should be distinguished from measurement-noise whitening. If C_q denotes the covariance of the measurement error in $r_{q,k}$, the covariance of the normalized error is $\widetilde{C}_q = C_q / s_q^2$. For independent white measurement noise with variance σ_q^2, the inverse-variance weight depends on the noise variance after reference-RMS normalization. Inverse-variance weighting of the normalized residual block gives

$$w_q = \frac{1}{\sigma_q^2 / s_q^2} = \frac{s_q^2}{\sigma_q^2} \tag{20}$$

Accordingly, equal weights after RMS normalization coincide with inverse-variance relative weighting only when the two normalized noise variances are equal. A common rescaling of the data-fitting term must also be accompanied by a consistent rescaling of the regularization parameter to preserve the same regularized solution.

4.4. Controlled Solution Strategies

To separate the effects of ordinary inversion, regularization, physical bounds, and dynamic locking, four solution strategies are considered under the same outer nonlinear framework. At outer iteration k, all methods use the same residual vector r_k and the

same current sensitivity matrix S_k. Only the inner inverse subproblem is changed. This distinction is essential: a closed-form or SVD solution provides only the increment for the current linearized problem, whereas the damage model and sensitivity matrix are updated in the next outer step.

(1) Nonlinear ordinary least squares

The ordinary least-squares baseline minimizes the current linearized residual without regularization or explicit damage-factor bounds, consistent with Equation (13):

$$\Delta a_k^{\mathrm{OLS}} = \mathrm{argmin}_{\Delta a} \|r_k - S_k \Delta a\|_2^2 \tag{21}$$

The increment is obtained from the Moore–Penrose solution, implemented using an SVD-based pseudoinverse. The forward model is then updated and the response sensitivity is recomputed at a_{k+1}. Because the unconstrained update can produce negative damage factors or factors greater than one, the raw candidate is retained for diagnosis, while a positive-stiffness safeguard is applied before the next forward calculation.

Equivalently, if $S_k = U_k \Sigma_k V_k^{\mathrm{T}}$, the numerical update is $\Delta a_k^{\mathrm{OLS}} = V_k \Sigma_k^{+} U_k^{\mathrm{T}} r_k$, with singular values below the prescribed rank tolerance discarded.

(2) Nonlinear Tikhonov regularization

For comparison, the Tikhonov baseline applies zero-order regularization to the current linearized residual, analogous to the objective in Equation (15):

$$\Delta a_k^{\mathrm{T}} = \mathrm{argmin}_{\Delta a} \left\{ \|r_k - S_k \Delta a\|_2^2 + \lambda_k \|\Delta a\|_2^2 \right\} \tag{22}$$

For zero-order Tikhonov regularization, the SVD $S_k = U_k \Sigma_k V_k^{\mathrm{T}}$ gives:

$$\Delta a_k^{\mathrm{T}} = V_k \mathrm{diag}\left[\sigma_i / (\sigma_i^2 + \lambda_k) \right] U_k^{\mathrm{T}} r_k \tag{23}$$

At each outer iteration, the L-curve procedure described in Section 5.2 is applied to the current S_k and r_k to select λ_k before the next nonlinear model update.

(3) Nonlinear bounded least squares

The bounded least-squares baseline isolates the effect of physical damage bounds from the effect of Tikhonov regularization:

$$\Delta a_k^{\mathrm{B}} = \mathrm{argmin}_{\Delta a} \|r_k - S_k \Delta a\|_2^2, \ -a_k \le \Delta a \le 1 - a_k. \tag{24}$$

The state-dependent bounds are imposed on the increment rather than directly using fixed bounds on $\triangle_a$. This ensures that the updated state satisfies $0 \le a_{k+1} = a_k + \Delta a \le 1$ while still allowing a previously overestimated damage factor to decrease. The bounded linear subproblem is solved numerically by a trust-region reflective bounded least-squares solver, and the solver iteration count is recorded separately from the nonlinear outer iteration count.

(4) Proposed nonlinear bounded Tikhonov with dynamic locking

The proposed strategy combines bounded Tikhonov inversion with an outer dynamic locking rule. An unclipped diagnostic Tikhonov candidate is evaluated before the bounded update is determined:

$$\Delta a_k^{\mathrm{P}} = \mathrm{argmin}_{\Delta a} \left\{ \|r_k - S_{k,A} \Delta a\|_2^2 + \lambda_k \|\Delta a\|_2^2 \right\}, \ -a_{k,A} \le \Delta a \le 1 - a_{k,A}. \tag{25}$$

The locking test is applied before clipping to the feasible interval: the diagnostic candidate is $\widetilde{a}_{k+1} = a_k + T_k \Delta a_k^{\mathrm{diag}}$. A zone is locked only when its candidate is negative in three consecutive outer relinearization updates. If a locked zone currently has a nonzero

value, its fixed increment is $\Delta a_{k,\mathcal{F}} = -a_{k,\mathcal{F}}$, and the active right-hand side is corrected as $r_{k,\mathcal{A}} = r_k - S_{k,\mathcal{F}}\Delta a_{k,\mathcal{F}}$ before the bounded solve. The inner iterations of the bounded solver do not contribute to the three-update locking memory.

Following a locking event, the regularization parameter is reselected using the updated active set so that the subsequent inverse problem reflects the revised set of free damage factors.

For all four methods, the outer iteration terminates only when the applied damage update and the nonlinear forward residual satisfy their prescribed tolerances, or when the maximum number of outer iterations is reached. An additional no-lock bounded-Tikhonov calculation can be used as an ablation to distinguish the effect of dynamic locking from the effects of relinearization, regularization, and physical bounds.

5. Damage Identification of a Single-Span Simply Supported Bridge

5.1. Numerical Cases and Comparison Procedure

The numerical study evaluates both the inversion strategy and the response configuration using the vehicle–track–bridge model described above. The bridge span is 32 m, and the 50 finite elements are grouped into ten consecutive damage zones, each containing five elements [38]. The train speed and sampling frequency are 60 km/h and 400 Hz, respectively. The prescribed track-irregularity realization is retained, and Gaussian white noise with an RMS amplitude equal to 5% of the corresponding clean signal RMS is added to the response channels. The three prescribed damage cases are summarized in Table 3; all unlisted zones are undamaged. Along the bridge span, the bridge is divided into 10 damage zones, corresponding to 10 damage factors, as shown in Figure 5.

Table 3. Prescribed zone-level damage cases.

Case	Damaged Zones	Prescribed Damage Factors
Single damage	3	$\alpha_3 = 0.20$
Multiple damage	4 and 9	$\alpha_4 = 0.15$; $\alpha_9 = 0.20$
Minor damage	4 and 7	$\alpha_4 = 0.05$; $\alpha_7 = 0.10$

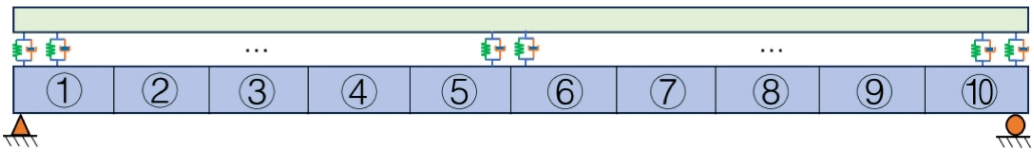


Figure 5. Bridge model and the ten damage zones used in the identification study.

Three observation configurations are considered for each damage case. The onboard-only configuration uses the leading-vehicle body pitch angular velocity, the bridge-only configuration uses the bridge mid-span vertical acceleration, and the joint configuration stacks the two response channels. For joint inversion, each channel is divided by its fixed intact-response RMS scale, as described in Section 4.3. The labels "Unit number" and "E.i" in the plots refer to the ten damage zones rather than to individual finite elements.

Each response configuration is evaluated using NL-OLS, NL-Tikhonov, NL-BoundedLS, and the proposed bounded-Tikhonov method with dynamic locking. Together, the three cases, three response configurations, and four solution strategies form 36 method–configuration comparisons. All four strategies employ outer nonlinear model updates and sensitivity recalculation; the "NL" prefix does not indicate a fixed-sensitivity, single-step inversion. The prescribed damage factors provide a reference for assessing the results, not an input specifying which zones are active.

The bar charts compare the reported final damage distributions, whereas the iteration histories show the proposed method only. The histories contain the initial state and four displayed updates.

5.2. Single-Damage Identification

5.2.1. Onboard-Only Response

For the prescribed 20% stiffness reduction in zone 3, both the proposed method and NL-BoundedLS recover a dominant damage factor of approximately 0.19, with only very small remaining indications outside the damaged zone (Figure 6) NL-OLS underestimates zone 3 and produces much larger spurious peaks, particularly in zones 1 and 10. NL-Tikhonov also underestimates the damaged zone, at approximately 0.14, while retaining a prominent spurious indication in zone 1. Thus, regularization without physical bounds does not provide reliable localization for this onboard-only case. The proposed trajectory shows that zone 3 approaches 0.20 by the second displayed update and changes little after the third; the transient indications in zones 2 and 4 are largely removed. This is evidence of stabilization over the displayed updates.

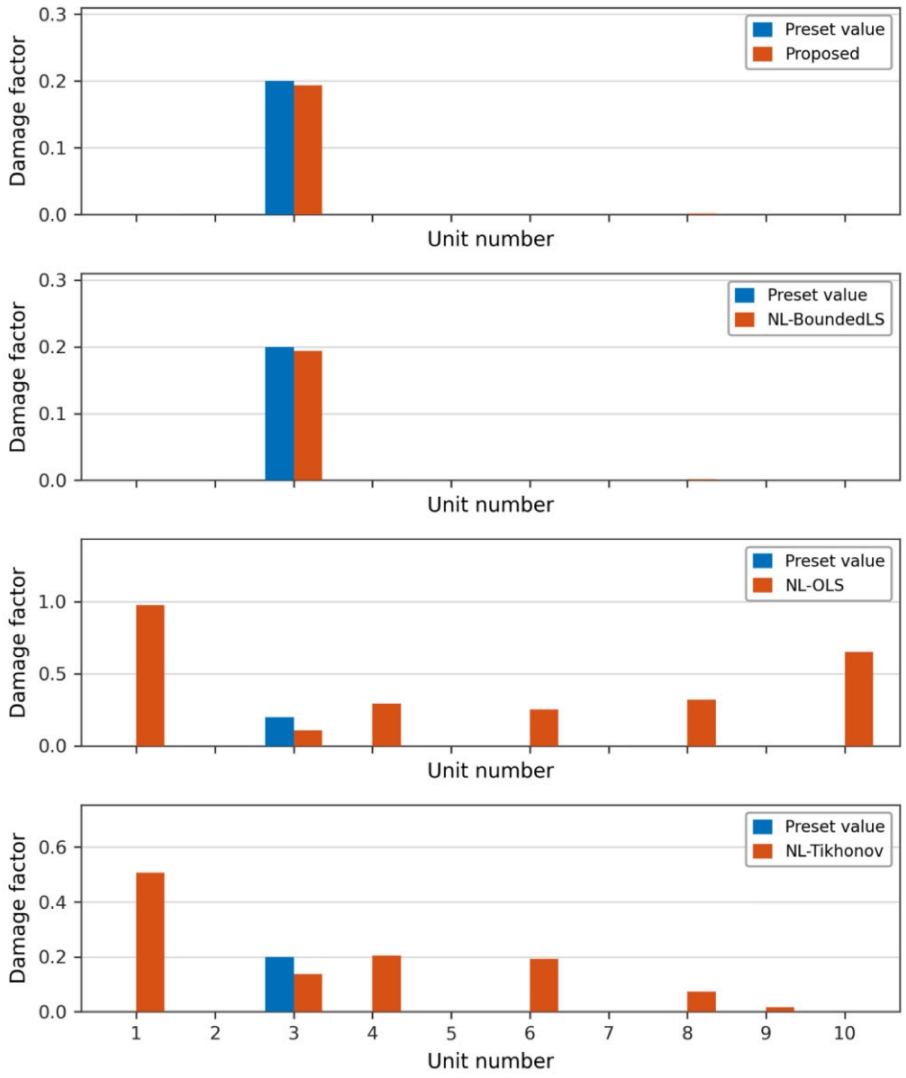


Figure 6. Single-damage identification: onboard-only response.

5.2.2. Bridge-Only Response

With the bridge mid-span acceleration alone, the proposed method identifies zone 3 at approximately 0.20, while small spurious indications remain in zones 1 and 7 (Figure 7). NL-

BoundedLS gives a closely comparable distribution. NL-Tikhonov identifies the damaged zone at approximately 0.22 but leaves additional nonzero estimates in several undamaged zones. In contrast, NL-OLS substantially underestimates zone 3 and distributes large positive estimates over undamaged zones. The proposed history shows a weak initial estimate of the actual damaged zone, followed by an increase to approximately 0.21 at the second update and a gradual reduction toward 0.20. The initial estimates in other zones decrease, although the small residual indication in zone 1 persists. Accordingly, the final distribution is concentrated near the correct location, but complete elimination of spurious damage is not supported.

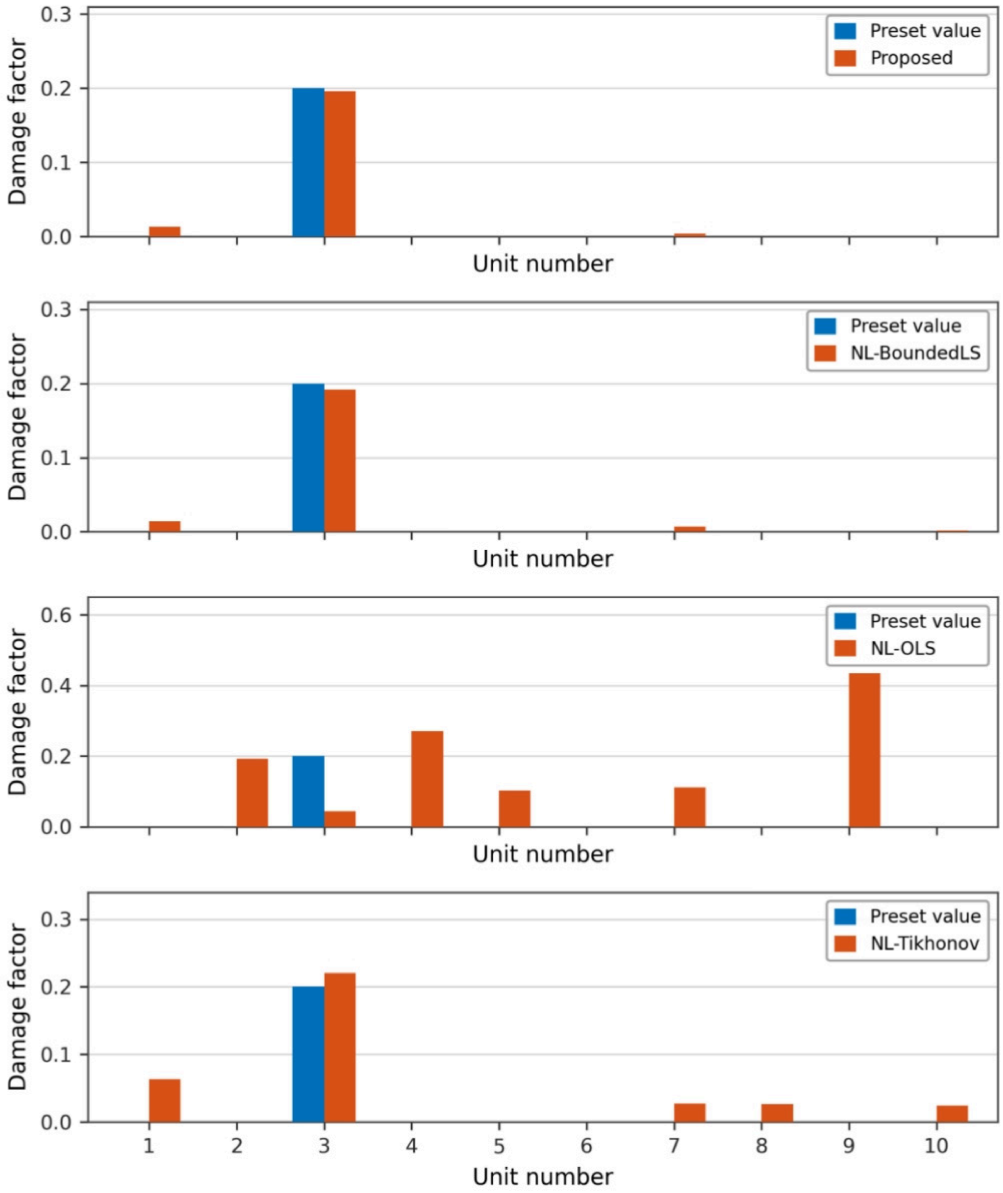


Figure 7. Single-damage identification: bridge-only response.

5.2.3. Joint Response

Joint use of the onboard and bridge measurements gives a proposed estimate very close to the prescribed factor of 0.20 in zone 3 (Figure 8). NL-BoundedLS produces a similarly concentrated distribution, with a slightly lower main estimate. NL-Tikhonov recovers the principal damaged zone but retains spurious indications, particularly in zones 1 and 10, whereas NL-OLS assigns substantial damage to several incorrect zones. Figure 9

presents the time histories of the damage factor for the single-damage scenario based on the proposed method. In the proposed iteration history (Figure 9), the estimate of zone 3 increases from a small initial value to approximately 0.13 at the second update and approximately 0.20 at the third. Transient estimates in adjacent zones then decrease substantially. The joint configuration provides a close severity estimate for this case, but the plotted distributions do not demonstrate a substantial or consistent advantage of the proposed method over NL-BoundedLS.

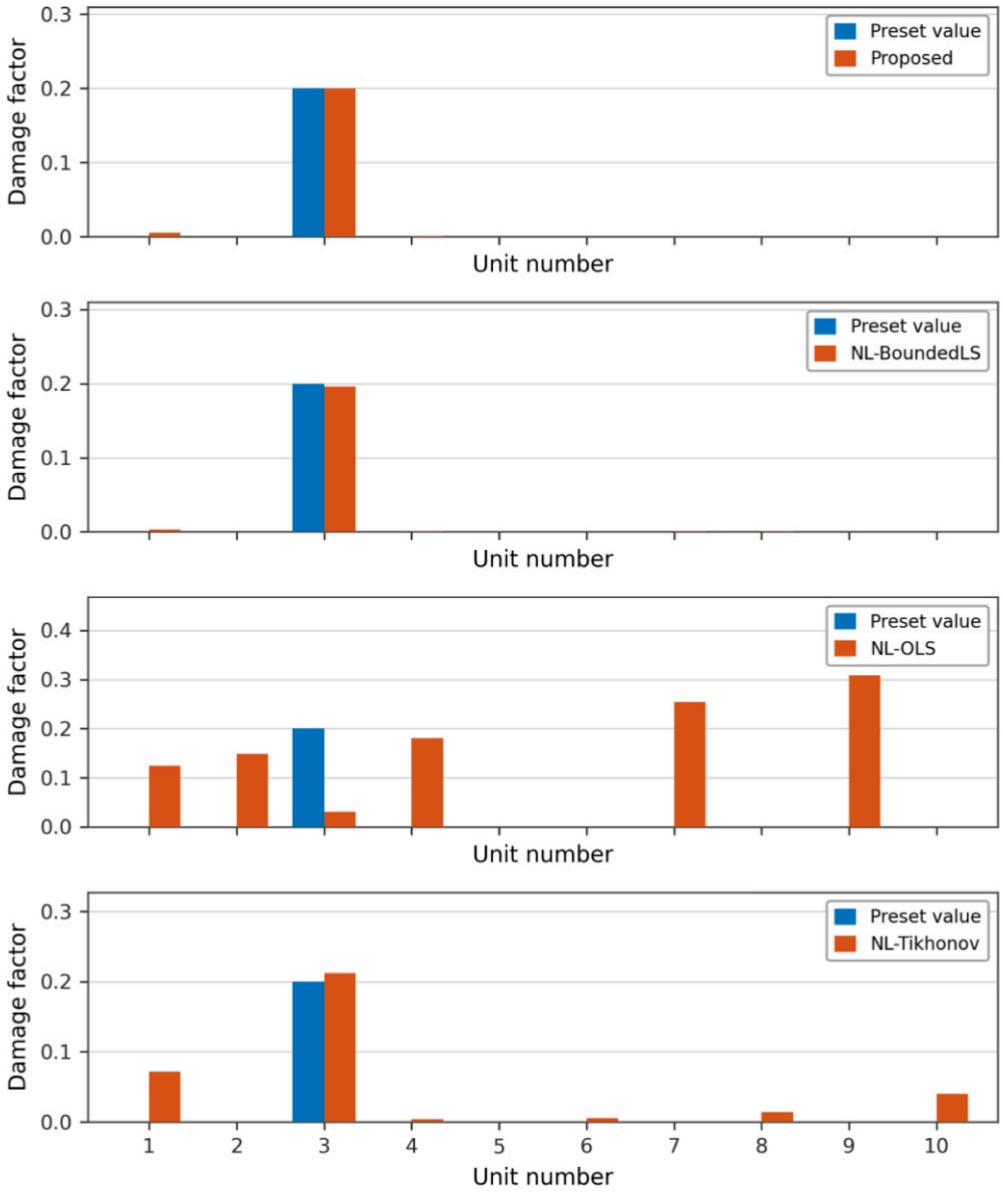


Figure 8. Single-damage identification: joint onboard–bridge response.

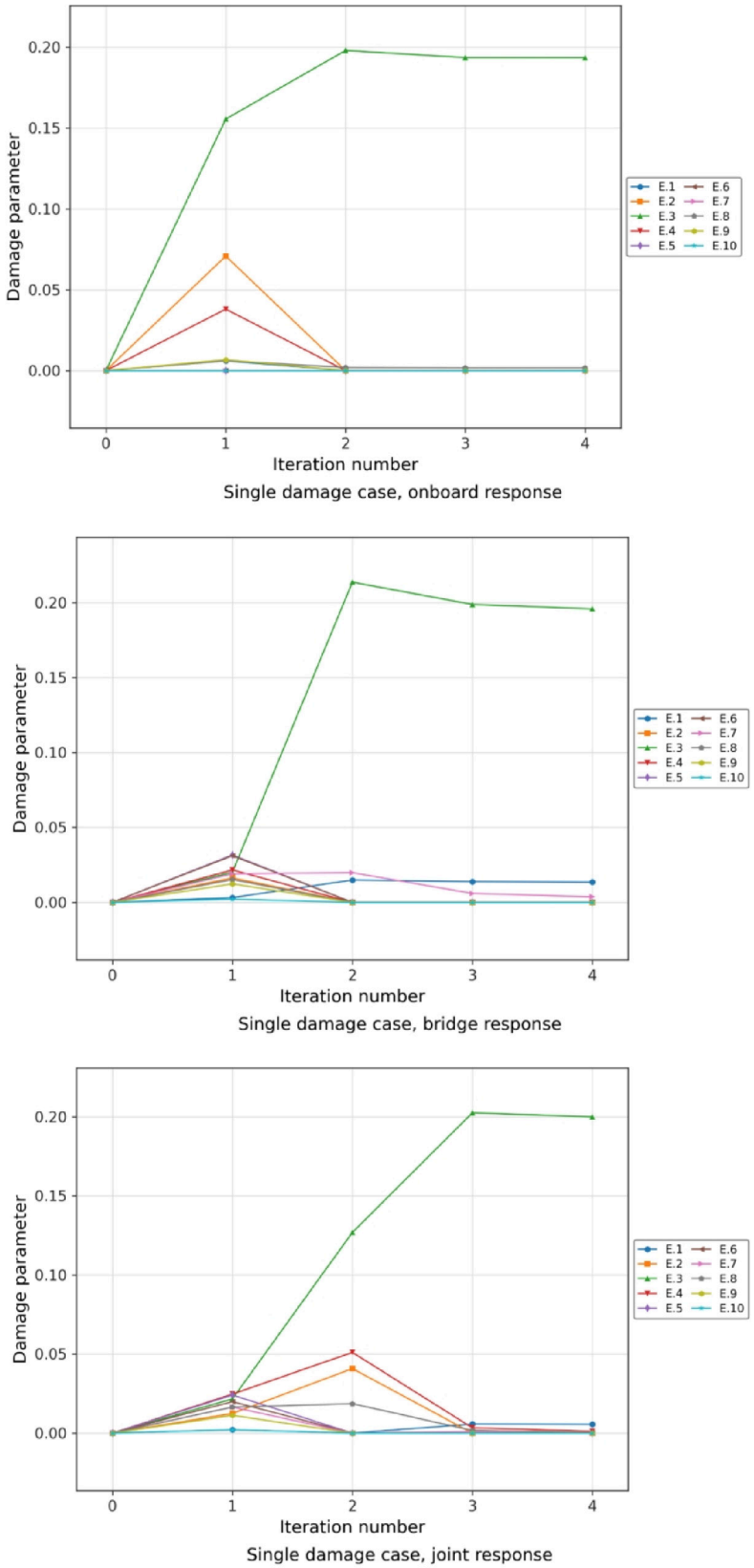


Figure 9. Proposed-method damage-factor histories for the single-damage case.

5.3. Multiple-Damage Identification

5.3.1. Onboard-Only Response

For the multiple-damage case, the prescribed factors are 0.15 in zone 4 and 0.20 in zone 9. The proposed onboard-only estimates are approximately 0.145 and 0.20, respectively,

and the remaining zones are near zero at the scale of the plot (Figure 10). NL-BoundedLS produces almost the same pattern. NL-OLS and NL-Tikhonov both retain substantial spurious damage, particularly in zone 1, and overestimate the damage in zone 4. The proposed history shows that the two damaged zones are already prominent after the first update. The transient estimates in zones 3, 5, 8, and 10 are largely removed at the second update, while zone 9 adjusts from an initial underestimate to a value close to 0.20. The last two displayed states are nearly unchanged. This case demonstrates that onboard-only identification can perform well for the tested larger damage factors.

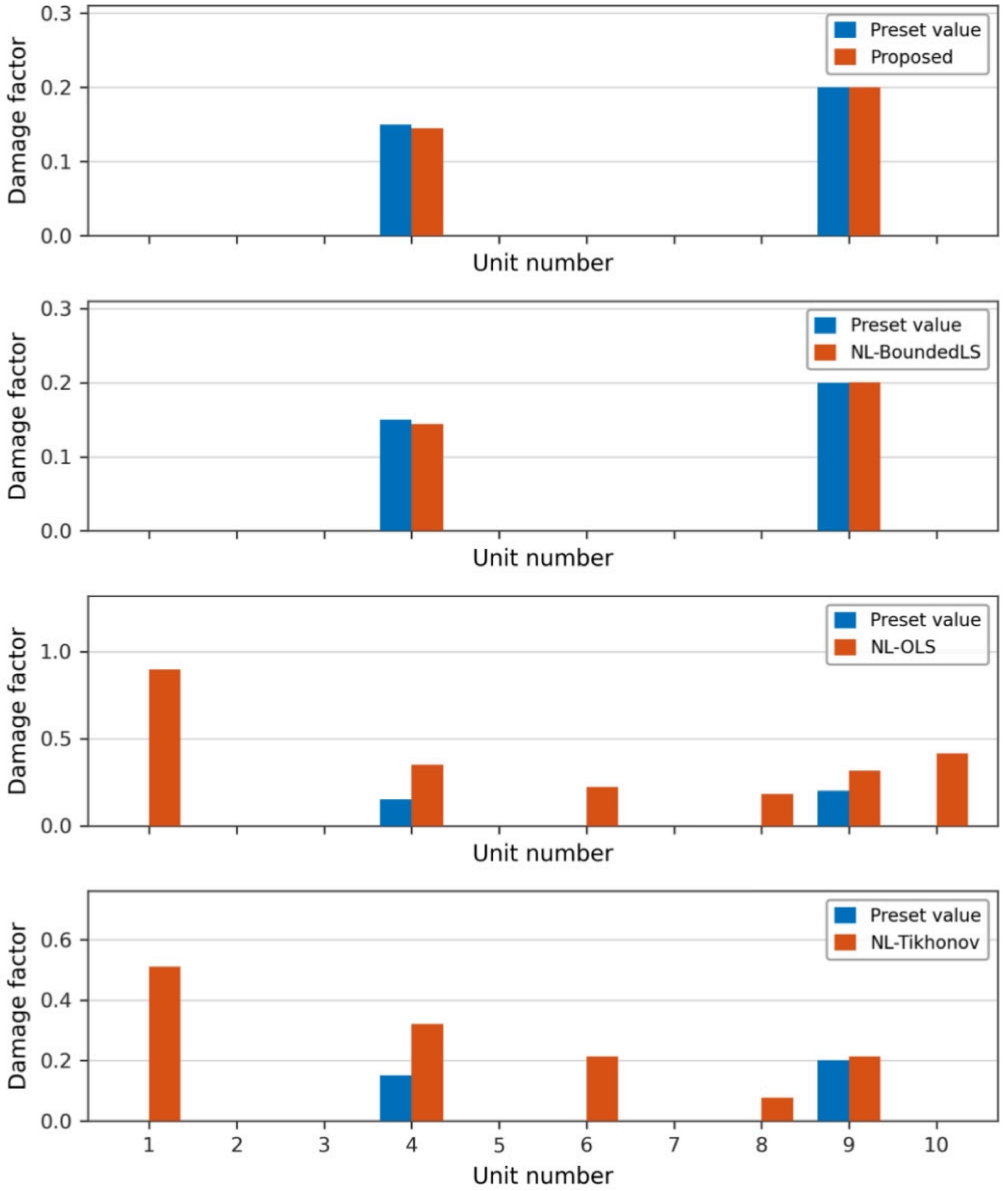


Figure 10. Multiple-damage identification: onboard-only response.

5.3.2. Bridge-Only Response

For bridge-only measurements, the proposed method underestimates both damaged zones, giving approximately 0.12 and 0.18 in zones 4 and 9 (Figure 11). Spurious indications of roughly 0.03–0.04 remain in zones 1, 7, and 10. NL-BoundedLS gives a similar distribution, showing that physical bounds alone do not remove all ambiguity in this configuration. NL-OLS and NL-Tikhonov overestimate the principal damage factors and produce an additional prominent indication in zone 2. The proposed method reduces the initially

large spurious estimate in zone 3, but other nonzero estimates appear and persist during subsequent updates. The main damage factors change only moderately toward the end of the displayed history while remaining biased. Consequently, stabilization of the iterates should not be equated with accurate recovery of the prescribed damage distribution.

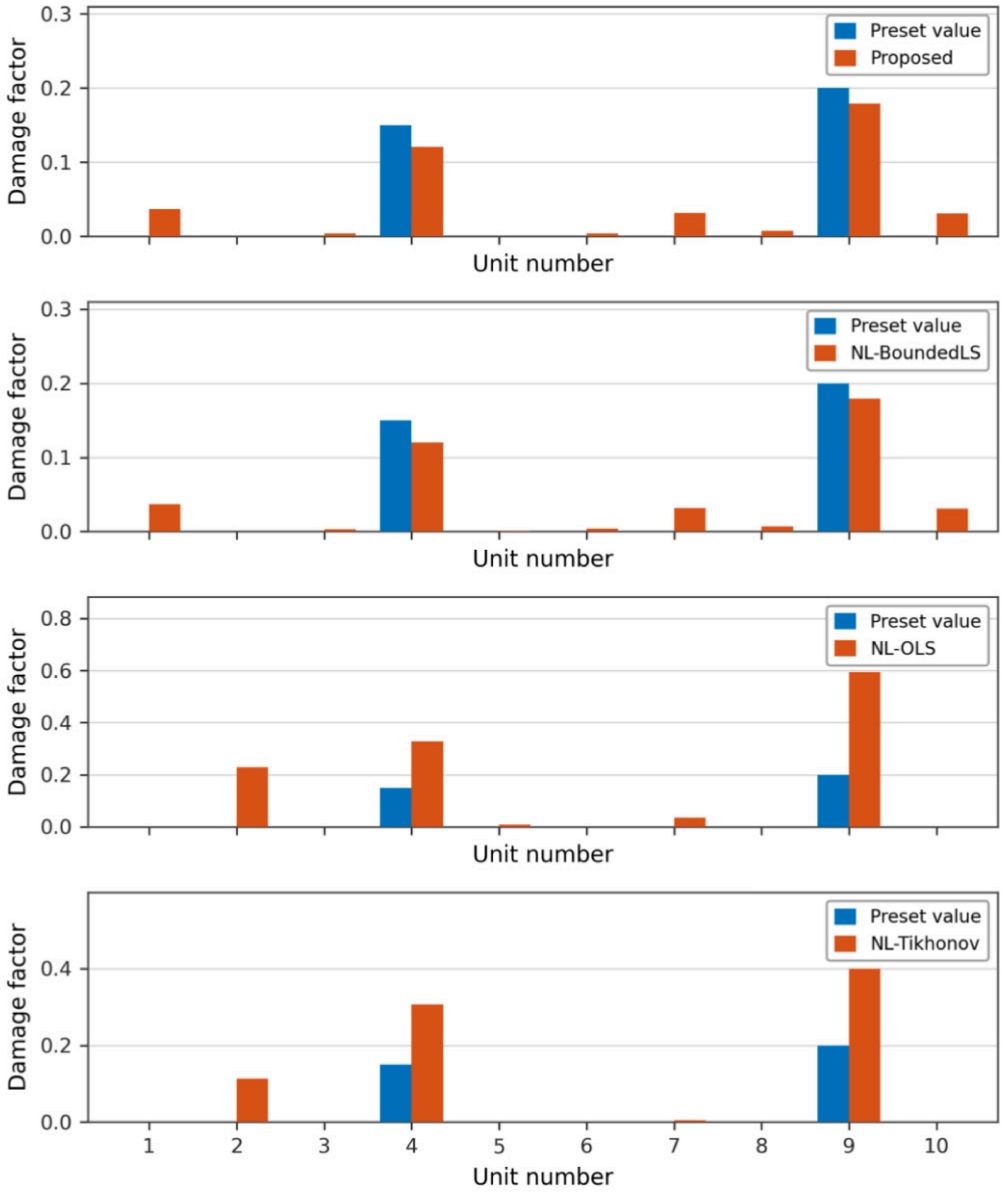


Figure 11. Multiple-damage identification: bridge-only response.

5.3.3. Joint Response

The joint-response estimates obtained by the proposed method are approximately 0.148 and 0.195 in zones 4 and 9, respectively (Figure 12). These values are closer to the prescribed factors than the corresponding bridge-only estimates. Small spurious indications remain, most visibly in zone 10, and NL-BoundedLS again gives almost the same distribution. The unconstrained baselines remain problematic: NL-OLS strongly overestimates zone 9, while NL-Tikhonov assigns a large spurious factor, approximately 0.90, to undamaged zone 10. Figure 13 shows the histories of the damage factor obtained by the proposed method under the multiple-damage case. The proposed history (Figure 13) shows initial overestimation of both damaged zones, followed by adjustment toward their final values by the third displayed update. Nevertheless, joint sensing is not uniformly superior to

onboard-only sensing in this case: the onboard-only estimate of zone 9 is closer to 0.20, and its undamaged-zone background is cleaner, whereas the joint estimate of zone 4 is closer to 0.15.

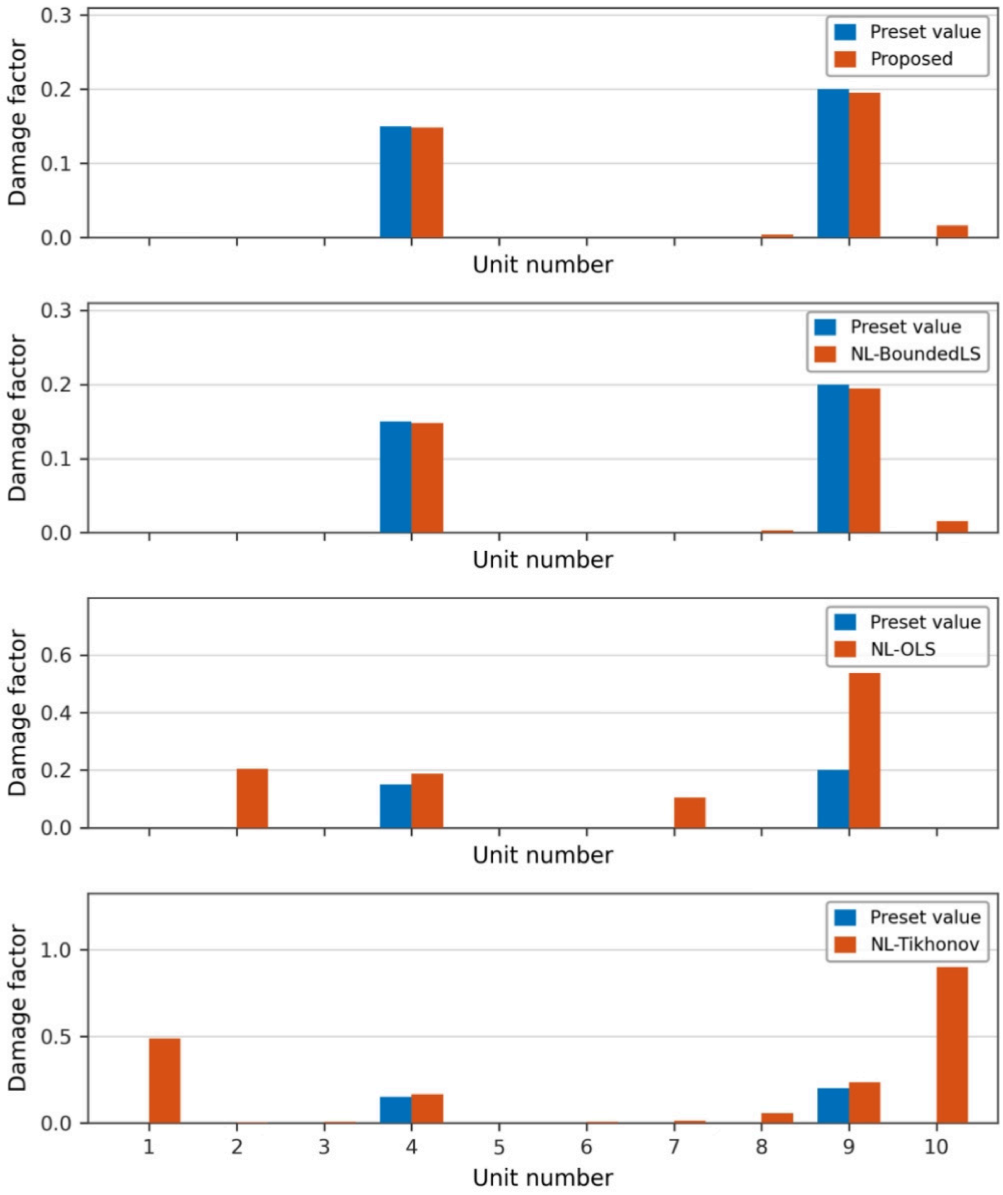


Figure 12. Multiple-damage identification: joint onboard–bridge response.

5.4. Minor-Damage Identification

5.4.1. Onboard-Only Response

The minor-damage case prescribes factors of 0.05 in zone 4 and 0.10 in zone 7. The final proposed onboard-only result does not recover this distribution reliably (Figure 14): zone 4 is underestimated at approximately 0.016, zone 7 is nearly zero, and substantial spurious factors appear in zones 1, 6, and 8. NL-BoundedLS performs distinctly better for the same configuration, identifying approximately 0.041 and 0.094 in the two damaged zones, with a small remaining indication in zone 8. The history is particularly important: the proposed estimates are already close to the prescribed factors at updates 2 and 3, but the fourth displayed update removes most of the zone-7 estimate and produces a large zone-1 peak. The reported final state must therefore be described as a late-iteration loss of identification

accuracy, not stable convergence. The histories alone do not establish whether this change originates from a locking event, another update decision, or the implementation.

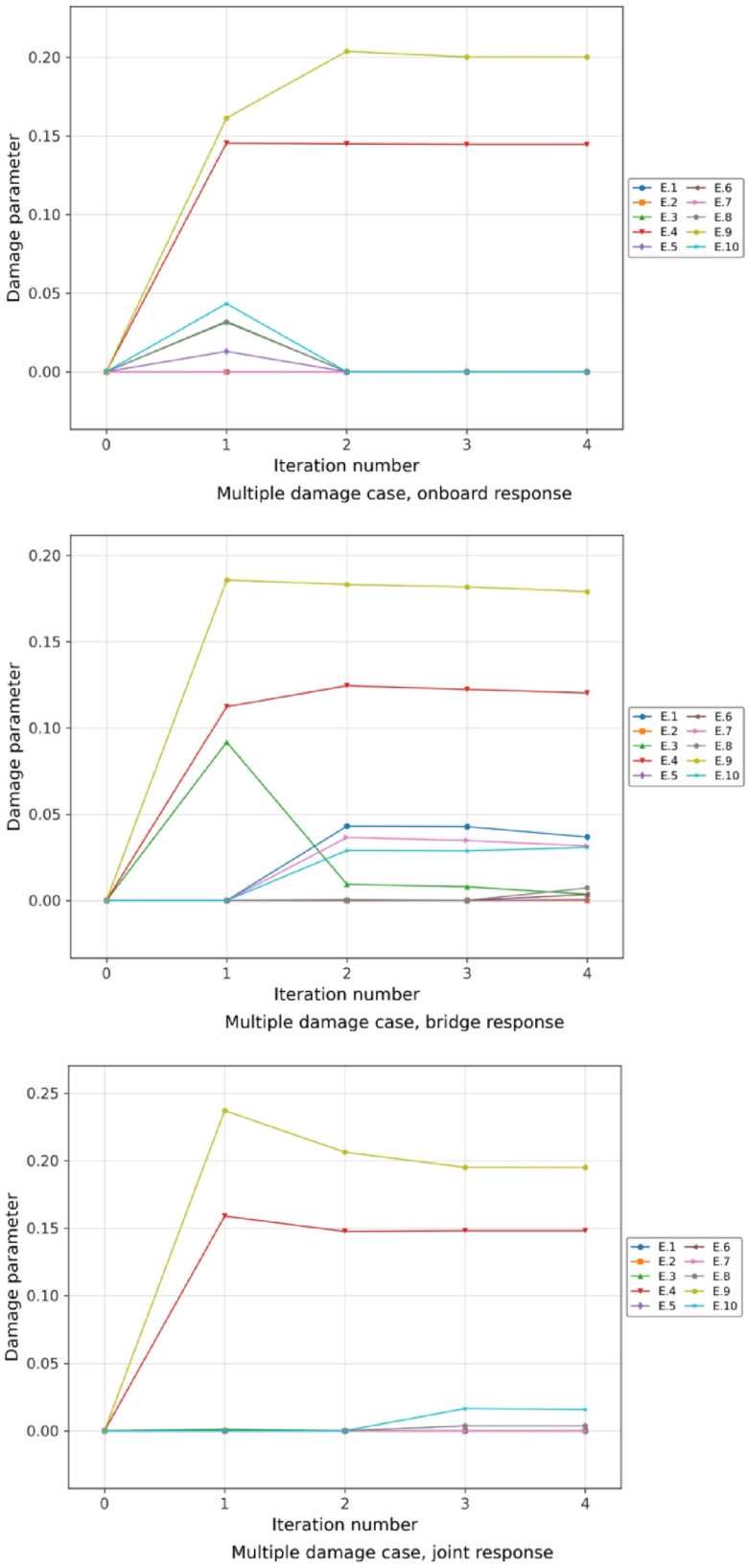


Figure 13. Proposed-method damage-factor histories for the multiple-damage case.

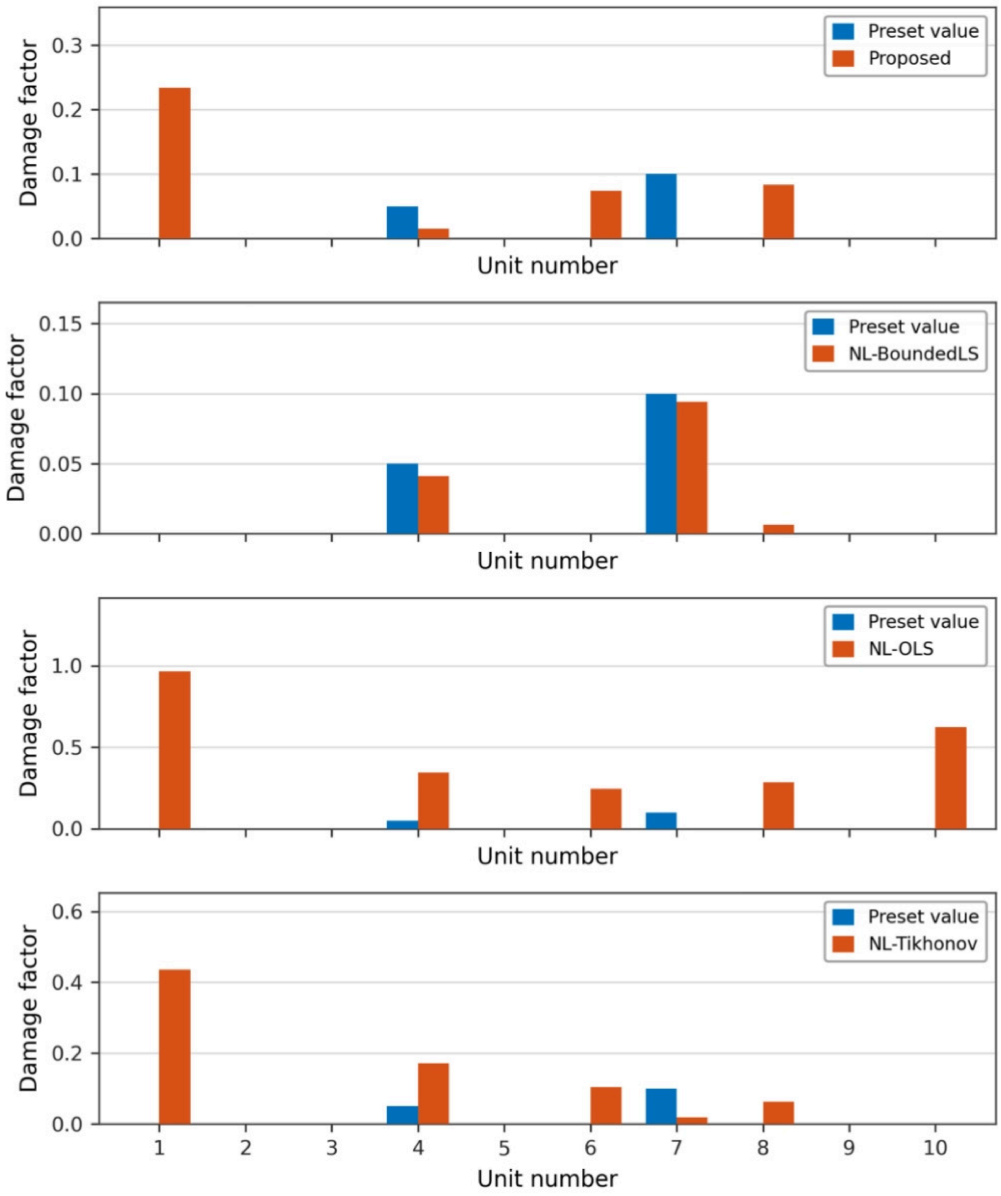


Figure 14. Minor-damage identification: onboard-only response.

5.4.2. Bridge-Only Response

The proposed bridge-only result retains both damaged zones, with approximate factors of 0.035 and 0.113 in zones 4 and 7, respectively (Figure 15). The locations are recovered, but the smaller damage is underestimated and the larger damage is overestimated. NL-BoundedLS yields essentially the same pattern. No prominent positive spurious bars are visible for these two methods at the plotted scale. NL-OLS produces large errors in damaged and undamaged zones, while NL-Tikhonov substantially underestimates zone 4 and retains several spurious indications. The proposed history shows that transient estimates in undamaged zones decrease toward zero. The two principal estimates settle near their reported final values during the last two displayed updates. Compared with the proposed onboard-only result, bridge-only identification avoids the severe loss of the zone-7 estimate, although a noticeable severity bias remains.

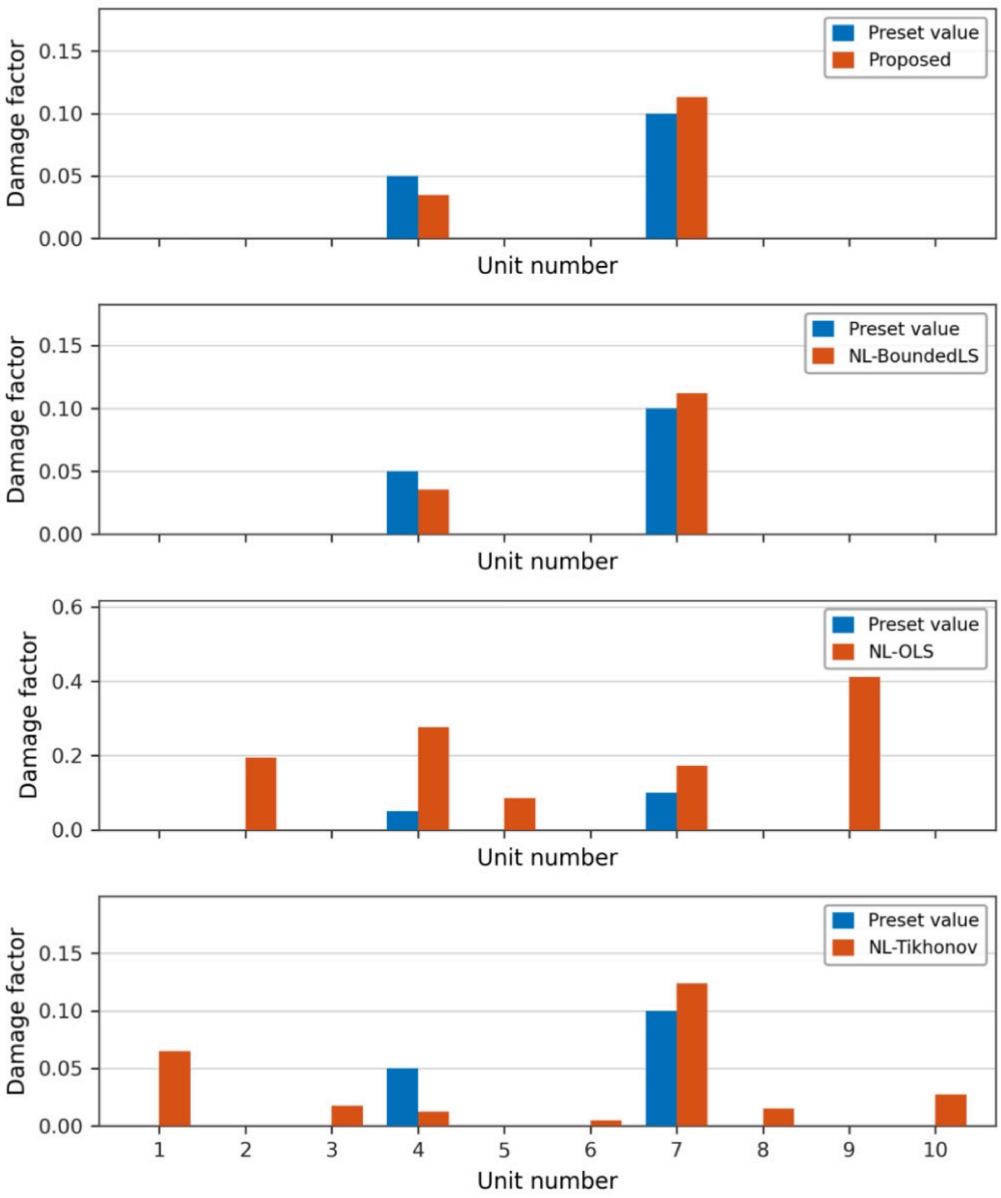


Figure 15. Minor-damage identification: bridge-only response.

5.4.3. Joint Response

For the proposed method, joint sensing gives the most accurate minor-damage distribution among the three response configurations shown (Figure 16). The estimated factors are approximately 0.048 and 0.101, close to the prescribed values of 0.05 and 0.10, and no prominent spurious indications are visible. NL-BoundedLS gives virtually the same result. In contrast, NL-OLS retains large spurious peaks, and NL-Tikhonov assigns substantial damage to undamaged zones 1 and 10 even though its estimates at the actual damaged zones are close to the reference values. The latter result illustrates why severity estimates at the known damaged zones alone are insufficient to assess identification quality. Figure 17 shows the histories of the damage factor obtained by the proposed method under the minor-damage case.The proposed trajectory shows that the two damaged zones are identified after the first update and adjusted slightly thereafter, without the abrupt final deterioration observed in the onboard-only case. The demonstrated benefit is therefore specific to the response configuration and the tested minor-damage realization.

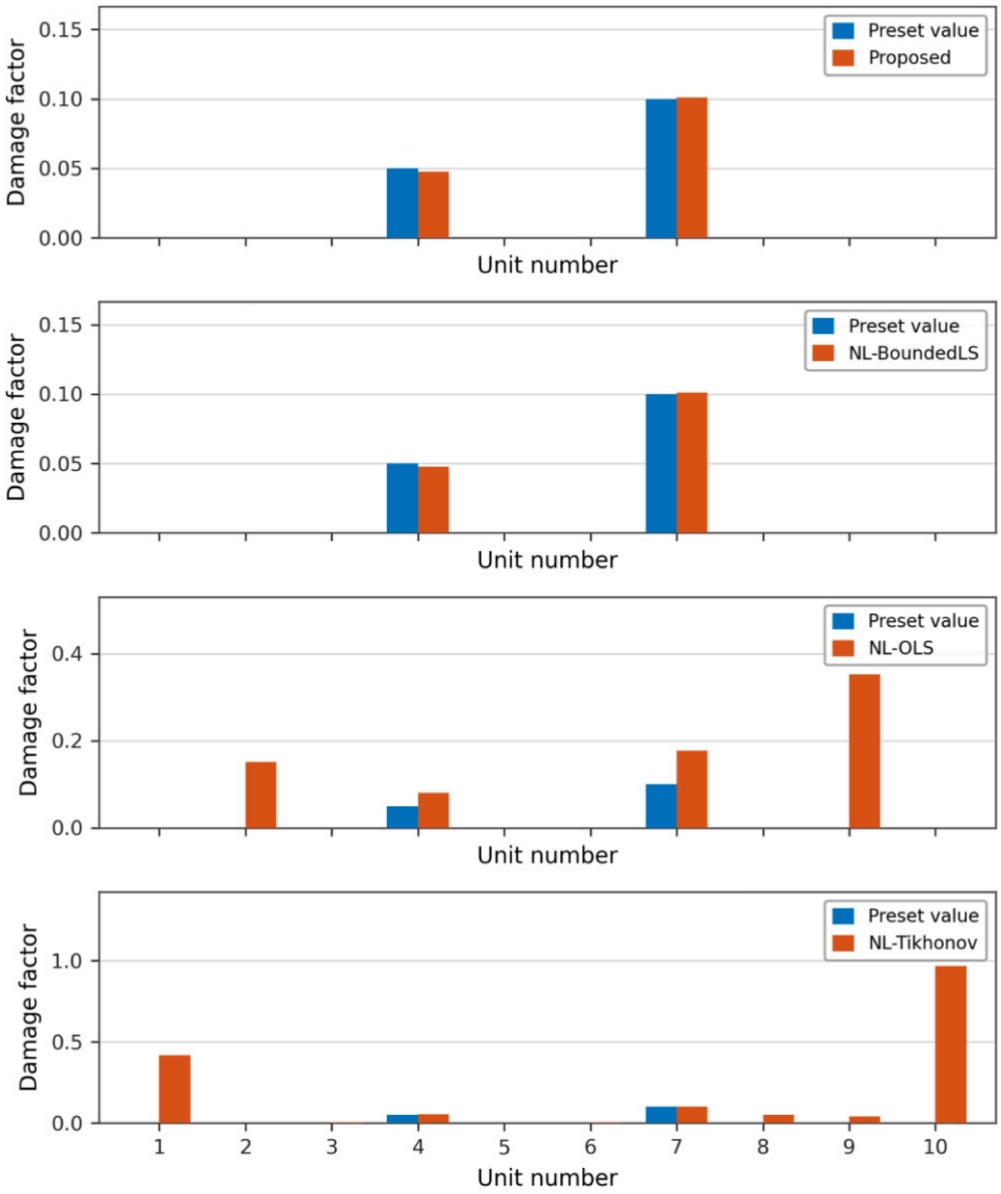


Figure 16. Minor-damage identification: joint onboard–bridge response.

5.5. Effect of Train Speed on Damage Identification

To examine the influence of train speed on damage identification, the proposed method is assessed at 40, 60, and 80 km/h for the single-, multiple-, and minor-damage cases defined in Table 3. The prescribed damage locations and factors are unchanged across the three speeds. Figures 10–12 compare the prescribed and identified zone-level damage factors. The assessment considers both the recovery of the damaged-zone factors and the magnitude of spurious indications in undamaged zones.

5.5.1. Single-Damage Case

For the single-damage case, the dominant identified peak remains in zone 3 at all three speeds (Figure 18). The estimated factor is approximately 0.195 at 40 km/h and remains close to the prescribed value of 0.20 at 60 and 80 km/h. The estimates in the remaining zones are small relative to the main damage peak. At 80 km/h, a spurious indication of approximately 0.01 appears in zone 1, but it does not obscure the location of the prescribed damage. These results indicate that damage localization is maintained at the three investigated speeds, with only small changes in the estimated damage severity.

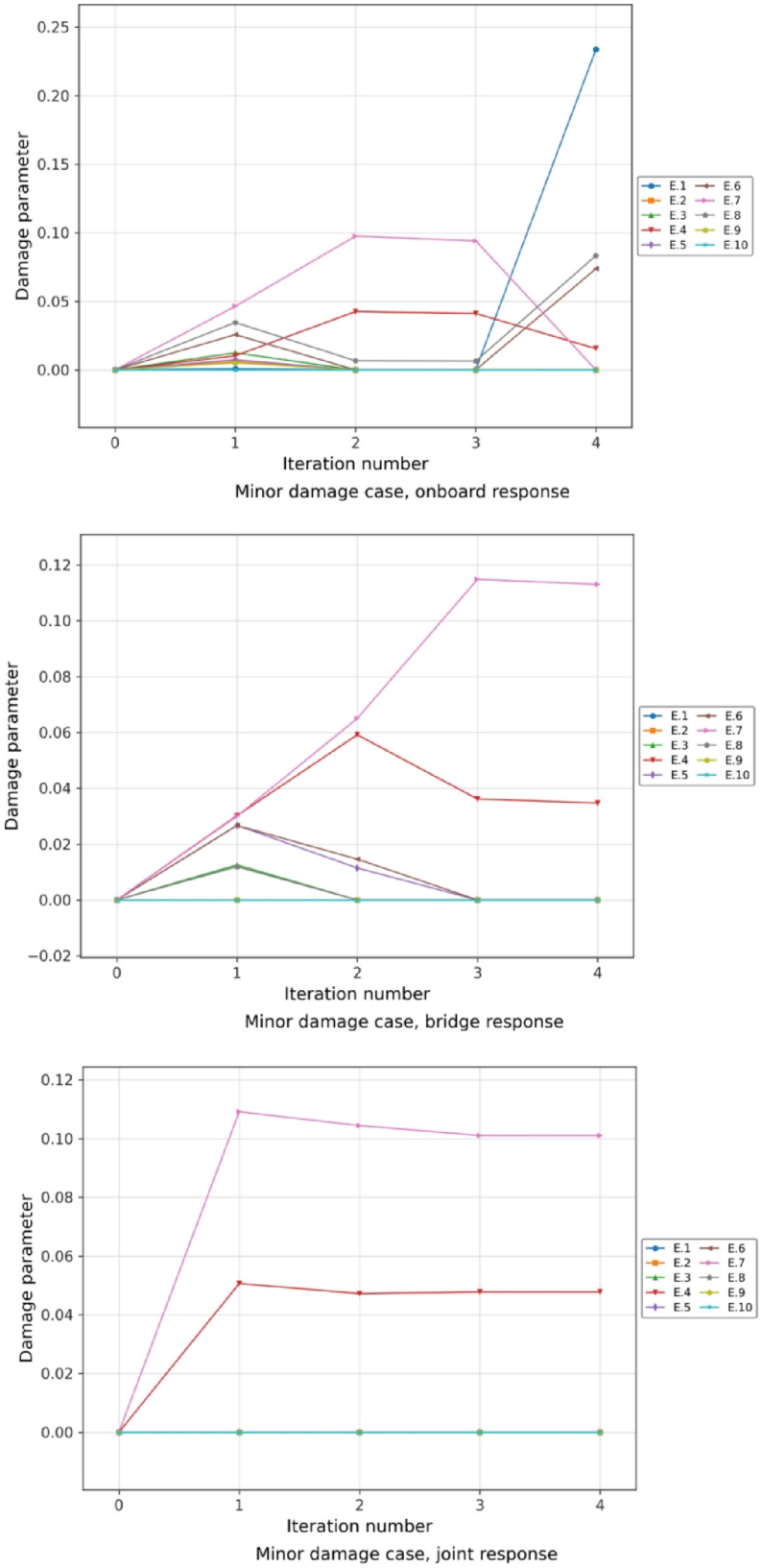


Figure 17. Proposed-method damage-factor histories for the minor-damage case.

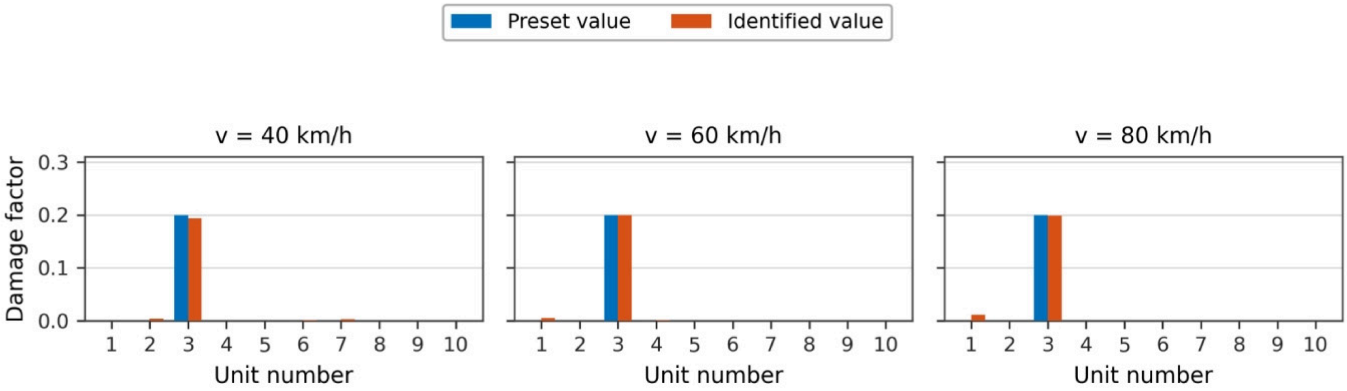


Figure 18. Single-damage identification by the proposed method at train speeds of 40, 60, and 80 km/h.

5.5.2. Multiple-Damage Case

For the multiple-damage case, the two principal peaks remain in zones 4 and 9 at all three speeds, corresponding to prescribed factors of 0.15 and 0.20, respectively (Figure 19). At 40 km/h, the identified factors are approximately 0.14 and 0.18, indicating underestimation of both damage severities. The estimates at 60 km/h are closer to the prescribed values, whereas slight underestimation remains at 80 km/h. Spurious indications are also present in several undamaged zones. In particular, the estimate in zone 10 reaches approximately 0.045 at 80 km/h and is more pronounced than the spurious peaks observed at the other two speeds. Thus, the main damage locations are retained, but the suppression of spurious indications varies with speed. Among the three speeds examined, 60 km/h provides the closest recovery of the two prescribed damage factors for this case.

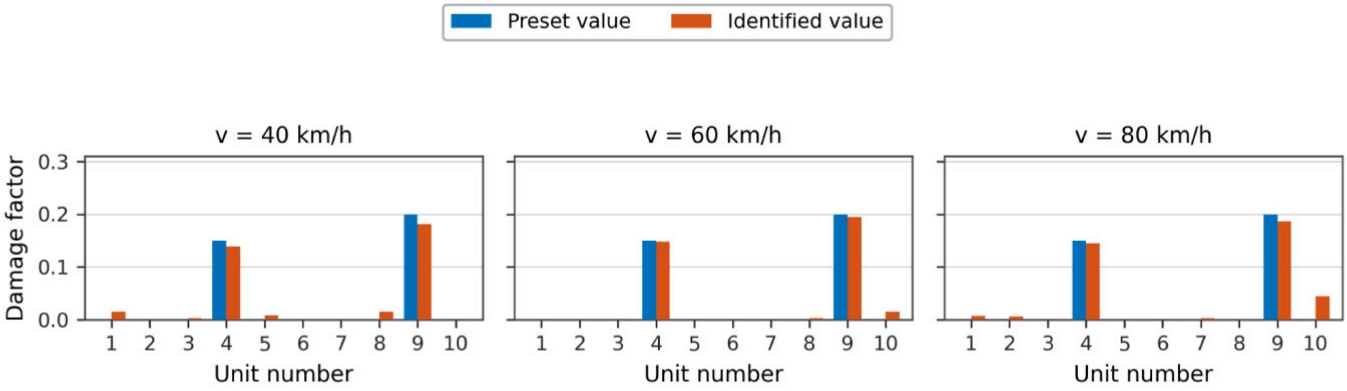


Figure 19. Multiple-damage identification by the proposed method at train speeds of 40, 60, and 80 km/h.

5.5.3. Minor-Damage Case

For the minor-damage case, the proposed method identifies the two prescribed damaged zones, namely zones 4 and 7, at each speed (Figure 20). The identified factors are approximately 0.044 and 0.103 at 40 km/h, 0.048 and 0.101 at 60 km/h, and 0.049 and 0.099 at 80 km/h, compared with prescribed values of 0.05 and 0.10. The underestimation of the smaller damage factor in zone 4 decreases over the three tested speeds, while the estimate in zone 7 remains close to its prescribed value. The remaining zones exhibit only very small nonzero estimates at the scale of the plots.

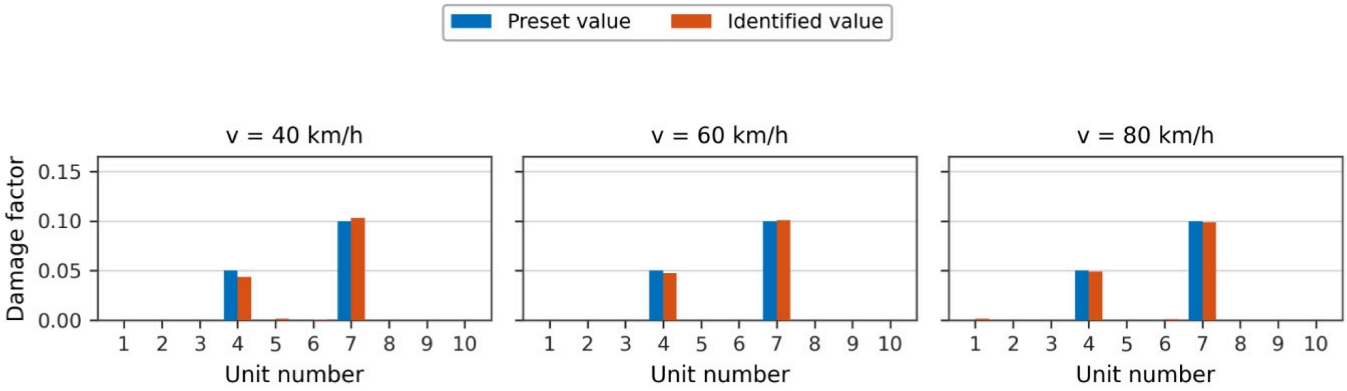


Figure 20. Minor-damage identification by the proposed method at train speeds of 40, 60, and 80 km/h.

Overall, the principal damage peaks remain at the prescribed locations at all three investigated speeds. However, the changes in severity estimates and spurious indications differ among the damage cases, and no common monotonic relationship between speed and identification accuracy is evident. The multiple-damage result at 80 km/h further shows that correct localization of the principal damage peaks does not imply complete suppression of spurious damage. These findings support the applicability of the proposed method at the tested speeds of 40, 60, and 80 km/h, rather than speed-independent performance. Additional speeds and repeated realizations are required to quantify the variability of identification accuracy beyond the reported comparisons.

5.6. Effect of Noise Level on Joint-Response Damage Identification

The influence of measurement noise is examined using the proposed method with joint vehicle–bridge responses, comprising the leading-vehicle body pitch angular velocity and the bridge mid-span vertical acceleration. Noise levels of 5%, 7%, and 10% are considered for the three damage cases in Table 3. Consistent with Section 2.3, noise level is expressed as the ratio of the RMS noise amplitude to the RMS amplitude of the corresponding clean response. Figures 13–15 show the final damage-factor distributions. The noise assessment is reported separately from the speed comparison in Section 5.5.

5.6.1. Single-Damage Case

For the single-damage case, zone 3 is identified at all three noise levels, and its estimated damage factor remains close to the prescribed value of 0.20 (Figure 21). The relative severity error increases from 0.0359% at 5% noise to 0.6900% at 7% noise and 1.6513% at 10% noise. No additional damaged zones are reported by the evaluation procedure. The relative L2 errors of the complete damage vector are 2.8319%, 3.10w%, and 1.6513%, respectively. Thus, the full-vector error does not increase monotonically with noise level: at 10% noise, the slightly larger error in zone 3 is accompanied by a reduction in the small undamaged-zone estimates visible at lower noise levels. This result does not imply that increasing noise improves identification performance.

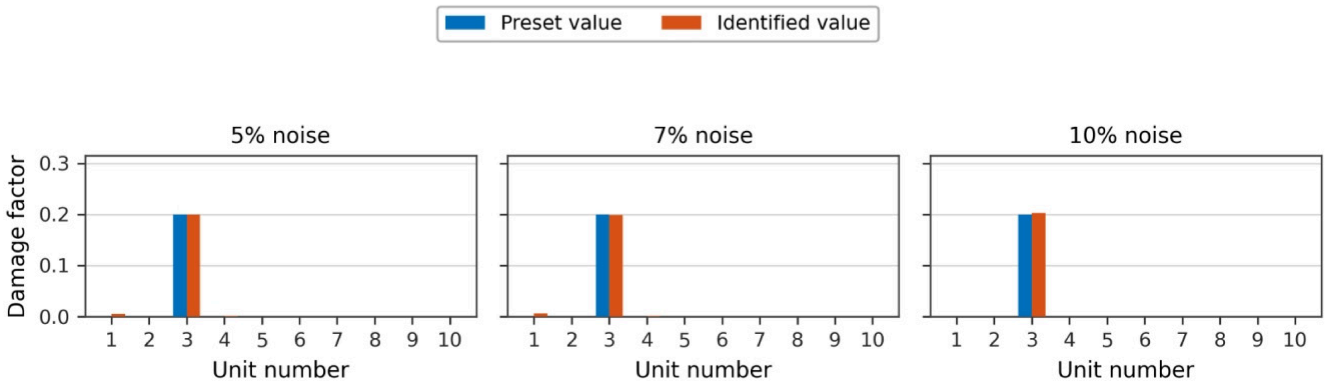


Figure 21. Single-damage identification by the proposed method using joint vehicle–bridge responses under 5%, 7%, and 10% noise levels.

5.6.2. Multiple-Damage Case

For the multiple-damage case, the two principal peaks remain in zones 4 and 9 at all three noise levels, corresponding to prescribed factors of 0.15 and 0.20 (Figure 22). The reported relative severity errors are 1.8867%, 3.6299%, and 3.5914% at 5%, 7%, and 10% noise, respectively. Although the severity errors at 7% and 10% noise are similar, the error in the complete spatial distribution continues to increase: the relative L2 error rises from 6.8269% to 16.6019% and then to 24.0341%. The plots show an increasingly pronounced spurious estimate in zone 10, reaching approximately 0.04 at 7% noise and 0.06 at 10% noise. The recorded detected-zone set consequently changes from {4, 9} at 5% noise to {4, 9, 10} at both higher noise levels, with one false positive in each case. Accordingly, recovery of the two true damage locations is maintained, but the estimated number of damaged zones and the overall damage distribution become less accurate.

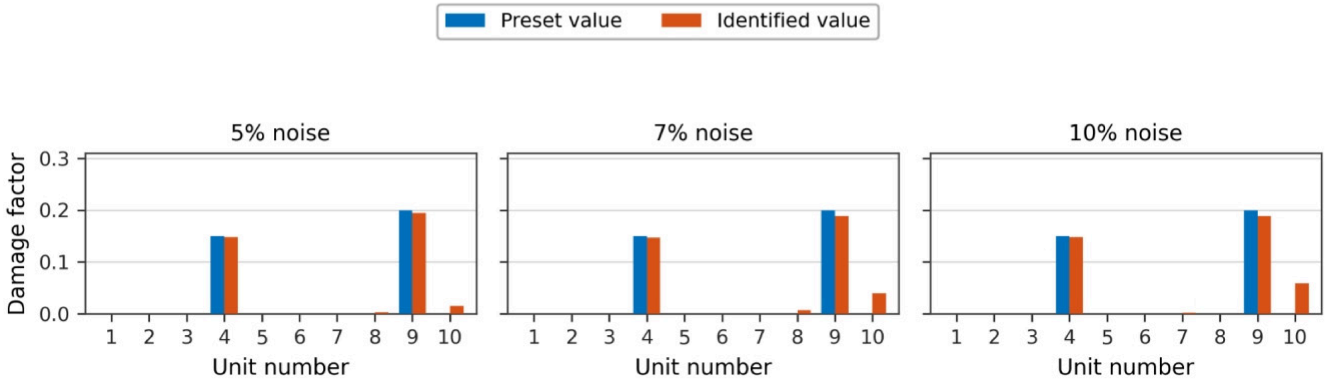


Figure 22. Multiple-damage identification by the proposed method using joint vehicle–bridge responses under 5%, 7%, and 10% noise levels.

5.6.3. Minor-Damage Case

For the minor-damage case, zones 4 and 7 remain identifiable at all three noise levels, with no additional zones classified as damaged (Figure 23). Relative to the prescribed factors of 0.05 and 0.10, the smaller damage in zone 4 is increasingly underestimated, while the factor in zone 7 is slightly overestimated. The reported relative severity error increases from 2.7366% at 5% noise to 4.1105% at 7% noise and 6.7864% at 10% noise. The corresponding relative L2 errors are 2.1903%, 3.2905%, and 5.4504%. Thus, the investigated noise increase affects severity estimation more than localization in this case. Both prescribed damage locations remain distinguishable, but their quantitative estimates become progressively less accurate.

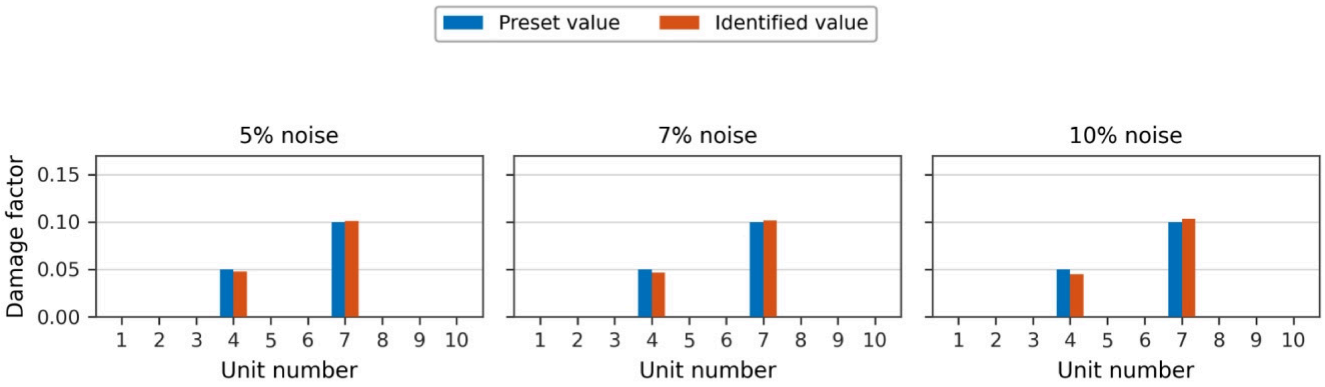


Figure 23. Minor-damage identification by the proposed method using joint vehicle–bridge responses under 5%, 7%, and 10% noise levels.

The recorded localization error is zero for all nine case–noise combinations. Nevertheless, the multiple-damage results at 7% and 10% noise contain an additional detected zone, demonstrating that zero localization error does not imply a completely correct detected damage set. The single- and minor-damage cases retain the prescribed detected-zone sets, whereas the multiple-damage case shows a greater increase in full-vector error. Identification quality therefore depends on both noise level and damage configuration and should be assessed using severity errors and undamaged-zone indications in addition to localization.

5.7. Effect of Track Irregularity on Joint-Response Damage Identification

The influence of track irregularity is assessed at a constant train speed of 60 km/h using the proposed method with joint vehicle–bridge responses. Three irregularity inputs are considered, labeled FRA class 6, class 5, and class 4, with recorded RMS amplitudes of 0.18, 0.27, and 0.54 mm, respectively. These RMS values characterize the simulated profiles used in this comparison. The prescribed damage locations and factors remain those specified in Table 3. Figures 16–18 compare the identified damage distributions.

5.7.1. Single-Damage Case

For the single-damage case, the dominant peak remains in zone 3 under all three irregularity inputs, and the estimated damage factor remains close to the prescribed value of 0.20 (Figure 24). The relative severity errors are 1.8291%, 0.0359%, and 1.8709% for classes 6, 5, and 4, respectively, with no additional zones classified as damaged. In contrast to the nonmonotonic variation in severity error, the relative L2 error of the complete damage vector increases from 1.8291% to 2.8319% and 3.5696%. The difference between these trends reflects the contribution of small estimates in undamaged zones to the full-vector error. Thus, the three inputs preserve the identified damage location but do not produce identical spatial distributions.

5.7.2. Multiple-Damage Case

For the multiple-damage case, the principal peaks remain in zones 4 and 9, corresponding to prescribed damage factors of 0.15 and 0.20 (Figure 25). The relative severity errors are 1.8890%, 1.8867%, and 2.1958% for classes 6, 5, and 4, respectively. Although the damaged-zone severity errors change only modestly, the relative L2 error increases from 6.3188% to 6.8269% and 9.8052%. A spurious estimate in zone 10 becomes more pronounced for the class-4 input. The recorded detected-zone set is {4, 9} for classes 6 and 5, but {4, 9, 10} for class 4, with one false positive. Therefore, both true damage locations are retained, while the higher-RMS input is associated with an overestimate of the number of damaged zones in this case.

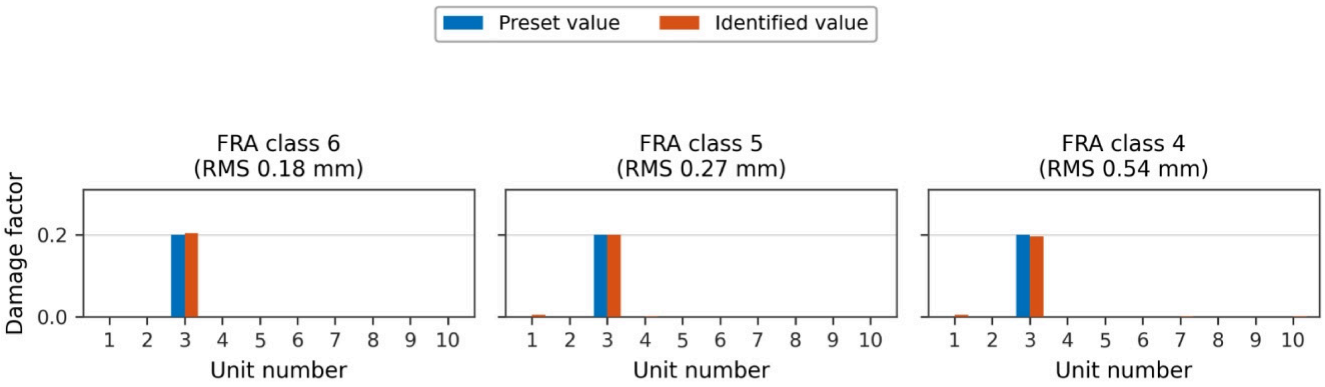


Figure 24. Single-damage identification by the proposed method using joint vehicle–bridge responses under FRA classes 6, 5, and 4 at 60 km/h.

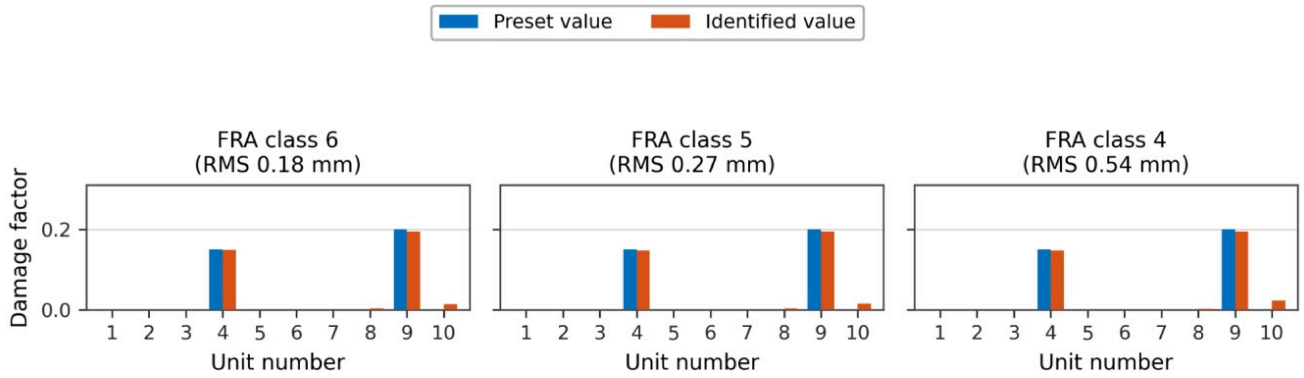


Figure 25. Multiple-damage identification by the proposed method using joint vehicle–bridge responses under FRA classes 6, 5, and 4 at 60 km/h.

5.7.3. Minor-Damage Case

For the minor-damage case, the prescribed damaged zones 4 and 7 remain identifiable under all three irregularity inputs, with no additional zones classified as damaged (Figure 26). The estimated factors remain close to the prescribed values of 0.05 and 0.10. As the recorded irregularity RMS increases from 0.18 to 0.27 and 0.54 mm, the relative severity error increases from 2.5362% to 2.7366% and 4.1015%, while the relative L2 error increases from 2.0290% to 2.1903% and 3.3136%. The plots indicate a greater underestimation of the smaller factor in zone 4 for the class-4 input, whereas the zone-7 estimate remains close to 0.10. The tested irregularity variation therefore affects the quantitative estimates without changing the detected damage locations in this case.

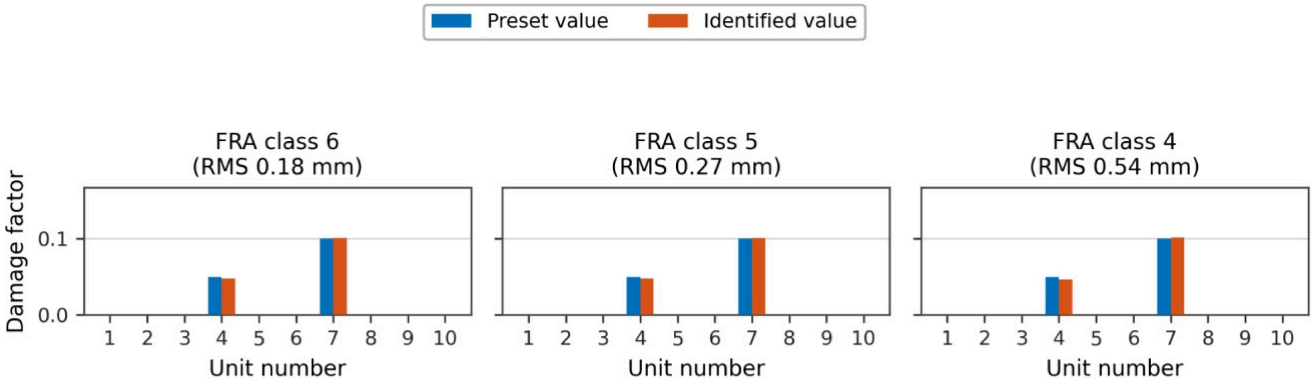


Figure 26. Minor-damage identification by the proposed method using joint vehicle–bridge responses under FRA classes 6, 5, and 4 at 60 km/h.

The recorded localization error is zero for all nine case–irregularity combinations. The detected-zone sets agree with the prescribed damage locations in eight combinations; the exception is the class-4 multiple-damage case, which includes the additional zone 10. The relative L2 error increases with the recorded irregularity RMS in each of the three damage cases, although the relative severity error is not uniformly monotonic. These results indicate that the principal damage locations remain recoverable for the tested inputs, while the accuracy of the complete spatial distribution depends on the irregularity condition and damage configuration.

6. Conclusions

Based on the vehicle-track-bridge coupled dynamic model, this paper developed a damage identification method for heavy-haul railway bridges, which takes train responses as the basis and vehicle-bridge interaction as the enhancement strategy. The main conclusions are as follows:

(1) A vehicle-track-bridge coupled dynamic model considering track-irregularity excitation was established, and a sensitivity equation for structural damage inversion was formulated with the pitch angular velocity response of the leading train as the observed quantity. To address the ill-posedness and ill-conditioning of the sensitivity equation, Tikhonov regularization and the L-curve method were introduced to determine the regularization parameter. Combined with engineering practice, a non-negativity constraint and dynamic locking constraint strategy for damage factors were proposed, forming a complete indirect damage identification method for bridges.

(2) Numerical examples of single-damage and multi-damage cases for a simply supported single-span bridge showed that under unconstrained conditions, the identification results could roughly locate damage but presented obvious false damage and even negative values, with errors spreading spatially. After the non-negativity constraint and dynamic locking constraint strategy were introduced, false damage was effectively suppressed, and both the location and severity of damage could be accurately identified. The stability and physical rationality of the identification results were significantly improved, and the algorithm converged smoothly under the interference of 5% Gaussian white noise.

(3) For minor damage cases with stiffness reductions of 5% and 10%, deviations existed in some sections when identification relied only on train responses, and false damage occurred in individual undamaged sections. After a vehicle-bridge cooperative identification method was constructed by combining the bridge mid-span acceleration response and the train body pitch angular velocity response, the location of minor damage could be accurately determined, and false identification was effectively suppressed. Compared with the method using single train responses, the vehicle-bridge cooperative method has obvious advantages in minor damage identification and noise resistance and is especially suitable for refined inspection of key bridges.

(4) The proposed method provides a potential approach for bridge damage detection using in-service trains. Train responses can be used as the primary information source for preliminary damage screening, while a small number of bridge measurement points can be introduced only when more refined damage identification is required. This strategy provides a possible basis for applying train-based monitoring to bridge inspection during routine railway operations.

The proposed damage identification framework based on train-response sensitivity shows potential for indirect condition assessment of heavy-haul railway bridges and large-scale railway inspection. The results highlight the importance of combining an appropriate constrained inversion strategy with an informative response configuration; however, the

findings remain limited to the numerical models and cases investigated. Further research is therefore required to improve numerical reliability, model fidelity, adaptability to complex service conditions, and practical applicability. Model refinement could subsequently include the development of a three-dimensional vehicle–track–bridge dynamic model incorporating lateral–vertical coupling, wheelset hunting motion, degradation of bridge lateral stiffness, and bridge torsional responses. More realistic representations of structural damage and nonlinear behavior, including breathing cracks and contact nonlinearities, could also be introduced to examine their effects on damage identifiability. Beyond the operating conditions considered in this study, systematic robustness assessments should include repeated independent realizations of measurement noise and track irregularity, a wider range of train speeds, environmental variations, and braking operations. For engineering validation, field train-crossing tests could be combined with existing bridge health monitoring data to evaluate the effects of model parameter uncertainties and field measurement noise, support model calibration, and assess the applicability of the identification algorithm under actual operating conditions. Finally, the integration of physics-based analytical methods with data-driven approaches, such as deep learning, could be explored to develop a hybrid damage identification framework that seeks to balance identification accuracy, computational efficiency, and practical applicability.

Author Contributions: S.Z., Investigation; writing—original draft preparation. Y.D., visualization; supervision; writing—review and editing. A.G., methodology; writing—review and editing. J.H., funding acquisition, writing—review and editing. All authors have read and agreed to the published version of the manuscript.

Funding: National Energy Shuohuang Railway Research Institute (Grant No.: 45 [2024]).

Institutional Review Board Statement: Not applicable.

Data Availability Statement: The original contributions presented in this study are included in the article. Further inquiries can be directed to the corresponding author.

Acknowledgments: The authors appreciate the financial support provided by the National Energy Shuohuang Railway Research Institute (Grant No.: 45 [2024]).

Conflicts of Interest: Authors Sheng Zhang and Yandong Dong are employed by the China Energy Transport Technology Research Institute Co., Ltd. The remaining authors declare that the research was conducted in the absence of any commercial or financial relationships that could be construed as a potential conflict of interest.

References

1. Zhou, M.; Liu, Y.; Wang, H.; Dong, H. Trajectory optimization for heavy-haul trains considering cyclic braking under complex operating conditions. *J. Rail Transp. Plan. Manag.* **2024**, *31*, 100462. [CrossRef]
2. Wang, D.; Su, J.; Luo, F.; Wang, Z.; Fan, J.; Luo, J.; Wang, G. Measurement of dynamic response and analysis of characteristics of heavy-haul railway tunnel bottom structure under train loading. *Buildings* **2025**, *15*, 3880. [CrossRef]
3. Lazorenko, G.; Kasprzhitskii, A.; Khakiev, Z.; Yavna, V. Dynamic behavior and stability of soil foundation in heavy haul railway tracks: A review. *Constr. Build. Mater.* **2019**, *205*, 111–136. [CrossRef]
4. Cui, S.; Shi, J. Estimating operation safety using an automatic peak detection method from monitoring signals of heavy-haul railway. *Transp. Saf. Environ.* **2025**, *7*, tdaf013. [CrossRef]
5. Cawley, P.; Adams, R.D. The location of defects in structures from measurements of natural frequencies. *J. Strain Anal. Eng. Des.* **1979**, *14*, 49–57. [CrossRef]
6. Catbas, F.N.; Gul, M.; Burkett, J.L. Damage assessment using flexibility and flexibility-based curvature for structural health monitoring. *Smart Mater. Struct.* **2007**, *17*, 015024. [CrossRef]
7. Pandey, A.K.; Biswas, M. Damage detection in structures using changes in flexibility. *J. Sound Vib.* **1994**, *169*, 3–17. [CrossRef]
8. Ratcliffe, C.P. Damage detection using a modified Laplacian operator on mode shape data. *J. Sound Vib.* **1997**, *204*, 505–517. [CrossRef]

9. Stubbs, N.; Kim, J.T.; Topole, K.G. The effect of model uncertainty on the accuracy of global nondestructive damage detection in structures. In *Computational Stochastic Mechanics*; Springer: Dordrecht, The Netherlands, 1991; pp. 157–168.
10. Beskhyroun, S.; Oshima, T.; Mikami, S. Wavelet-based technique for structural damage detection. *Struct. Control Health Monit.* **2010**, *17*, 473–494. [CrossRef]
11. Sony, S.; Gamage, S.; Sadhu, A.; Samarabandu, J. Vibration-based multiclass damage detection and localization using long short-term memory networks. *Structures* **2022**, *35*, 436–451. [CrossRef]
12. Nayek, R.; Narasimhan, S. Extraction of contact-point response in indirect bridge health monitoring using an input estimation approach. *J. Civ. Struct. Health Monit.* **2020**, *10*, 815–831. [CrossRef]
13. Li, J.; Zhu, X.; Guo, J. Enhanced drive-by bridge modal identification via dual Kalman filter and singular spectrum analysis. *Struct. Control Health Monit.* **2022**, *29*, e2927. [CrossRef]
14. Zhang, B.; Qian, Y.; Wu, Y.; Yang, Y.B. An effective means for damage detection of bridges using the contact-point response of a moving test vehicle. *J. Sound Vib.* **2018**, *419*, 158–172. [CrossRef]
15. Rana, S.; Adhikary, S.; Tasnim, J. A statistical index based damage identification method of a bridge using dynamic displacement under moving vehicle. *Structures* **2022**, *43*, 79–92. [CrossRef]
16. Krishnanunni, C.G.; Rao, B.N. Indirect health monitoring of bridges using Tikhonov regularization scheme and signal averaging technique. *Struct. Control Health Monit.* **2021**, *28*, e2686. [CrossRef]
17. Zhan, Y.; Au, F.T.K.; Zhang, J. Bridge identification and damage detection using contact point response difference of moving vehicle. *Struct. Control Health Monit.* **2021**, *28*, e2837. [CrossRef]
18. Zhan, J.; Xia, H.; Chen, S.; De Roeck, G. Structural damage identification for railway bridges based on train-induced bridge responses and sensitivity analysis. *J. Sound Vib.* **2011**, *330*, 757–770. [CrossRef]
19. Carnevale, M.; Collina, A.; Peirlinck, T. A Feasibility Study of the Drive-By Method for Damage Detection in Railway Bridges. *Appl. Sci.* **2019**, *9*, 160. [CrossRef]
20. Shi, J.; Shi, H.; Wu, Z.; Li, J. An on-board damage detection method for heavy-haul railway bridge based on sensitivity analysis of bogie responses. *IEEE Sens. J.* **2024**, *24*, 4642–4655. [CrossRef]
21. Shi, J.; Shi, H.; Wu, Z. An approach of on-board multistage health monitoring for heavy haul railway bridge using bogie acceleration. *Structures* **2023**, *57*, 105323. [CrossRef]
22. Liu, S.; Zhou, Z.; Zhang, Y.; Sun, Z.; Deng, J.; Zhou, J. Theoretical and Experimental Investigations of Identifying Bridge Damage Using Instantaneous Amplitude Squared Extracted from Vibration Responses of a Two-Axle Passing Vehicle. *Buildings* **2024**, *14*, 1428. [CrossRef]
23. Massarelli, E.; Raimondi, M.; Mara, S.; Civera, M.; Aimar, M.; Giordano, P.F.; Coletta, D.; Chiola, D.; Carambia, B.; Limongelli, M.P.; et al. Output-only modal analysis and system identification for indirect bridge health monitoring: Needs, requirements, and limitations. In *Proceedings of the 10th International Operational Modal Analysis Conference (IOMAC 2024)*; Springer: Cham, Switzerland, 2024; Volume 515. [CrossRef]
24. Massarelli, E.; Civera, M.; Mara, S.; Raimondi, M.; Giordano, P.F.; Quqa, S.; Aimar, M.; Limongelli, M.P.; Chiaia, B. Crowdsensing-based automated operational modal analysis for indirect bridge structural health monitoring. *Eng. Struct.* **2026**, *353*, 122203. [CrossRef]
25. Cronin, L.; Marasco, G.; Sen, D.; Dabbaghchian, I.; Matarazzo, T.; Pakzad, S. Bridge Modal Identification Using Crowdsourced Vibration Data from Passing Vehicles. In *Proceedings of the 10th International Operational Modal Analysis Conference (IOMAC 2024)*; Rainieri, C., Gentile, C., Aenlle López, M., Eds.; Lecture Notes in Civil Engineering; Springer: Cham, Switzerland, 2024; Volume 515. [CrossRef]
26. Matarazzo, T.J.; Kondor, D.; Milardo, S.; Eshkevari, S.S.; Santi, P.; Pakzad, S.N.; Buehler, M.J. Crowdsourcing bridge dynamic monitoring with smartphone vehicle trips. *Commun. Eng.* **2022**, *1*, 29. [CrossRef]
27. Song, J.; Lu, C.; Wang, A.; Wang, L.; Zang, A.; Vavryčuk, V.; Song, C.; Elsworth, D.; Zhang, X. Geophysical Observations and Numerical Modeling Constrain Mining-Induced Subsidence and Fault Reactivation: A Case Study. *Int. J. Rock Mech. Min. Sci.* **2026**, *204*, 106565. [CrossRef]
28. Sivasuriyan, A.; Vijayan, D.S.; Piętocha, A.; Górski, W.; Wodzyński, Ł.; Koda, E. Advanced Sensing and Digital Monitoring Technologies for Structural Health Assessment of Civil Infrastructure. *Buildings* **2026**, *16*, 656. [CrossRef]
29. Liu, W.; Tong, L.; Ma, W.; Xu, J. A Two-Stage Physics-Driven Graph Neural Network Framework for Predicting Tunneling-Induced Deformation of Frame Structures. *Can. Geotech. J.* **2026**, *63*, 1–22. [CrossRef]
30. Zhai, W.; Han, Z.; Chen, Z.; Ling, L.; Zhu, S. Train–track–bridge dynamic interaction: A state-of-the-art review. *Veh. Syst. Dyn.* **2019**, *57*, 984–1027. [CrossRef]
31. Xiao, Y.; Luo, X.; Liu, J.; Wang, K. Dynamic response of railway bridges under heavy-haul freight trains. *Adv. Civ. Eng.* **2020**, *2020*, 7486904. [CrossRef]
32. Song, L.; Liu, R.; Cui, C.; Yu, Z.; Zhang, W. Fatigue behavior of heavy-haul railway prestressed concrete beams based on vehicle-bridge coupling vibration. *Materials* **2022**, *15*, 2923. [CrossRef] [PubMed]

33. Greenberg, M.D. *Advanced Engineering Mathematics*; Prentice-Hall: Englewood Cliffs, NJ, USA, 1998.
34. Al-Bannagi, M.; Fang, K.; Kelamis, P.; Douglass, G. Acquisition footprint suppression via the truncated SVD technique. In Proceedings of the 74th Annual International Meeting, SEG Technical Program Expanded Abstracts, Denver, CO, USA, 10–15 October 2004; pp. 1957–1960.
35. Schmidt, M.; Fung, G.; Rosales, R. *Optimization Methods for l1-Regularization*; Technical Report TR-2009-19; University of British Columbia: Vancouver, BC, USA, 2009.
36. Burden, F.; Winkler, D. Bayesian regularization of neural networks. In *Artificial Neural Networks*; Methods in Molecular Biology; Humana Press: Totowa, NJ, USA, 2008; Volume 458, pp. 25–44.
37. Morozov, V.A. *Methods for Solving Incorrectly Posed Problems*; Springer Science & Business Media: New York, NY, USA, 2012.
38. Wang, X.; Zhuo, Y.; Li, S. Damage Detection of High-Speed Railway Box Girder Using Train-Induced Dynamic Responses. *Sustainability* **2023**, *15*, 8552. [CrossRef]

Disclaimer/Publisher's Note: The statements, opinions and data contained in all publications are solely those of the individual author(s) and contributor(s) and not of MDPI and/or the editor(s). MDPI and/or the editor(s) disclaim responsibility for any injury to people or property resulting from any ideas, methods, instructions or products referred to in the content.